
UNIVERSIDADE FEDERAL DE PERNAMBUCO
CENTRO DE TECNOLOGIA E |GEOCIÊNCIAS
DEPARTAMENTO DE ELETRÔNICA E SISTEMAS
PROGRAMA DE PÓS-GRADUAÇÃO EM ENGENHARIA ELÉTRICA

PEDRO HENRIQUE BEZERRA CAVALCANTI FILHO

# FREQUENCY DISCRIMINATORS BASED ON SIERPINSKI CURVE FRACTAL FSS FOR 4-BIT IFM SYSTEMS USING BALANCED BINARY CODE

Recife
2023

PEDRO HENRIQUE BEZERRA CAVALCANTI FILHO

# FREQUENCY DISCRIMINATORS BASED ON SIERPINSKI CURVE FRACTAL FSS FOR 4-BIT IFM SYSTEMS USING BALANCED BINARY CODE

Thesis presented to the Graduate Program in Electrical Engineering of the Federal University of Pernambuco, as a partial requirement for the title of Doctor in Electrical Engineering.

Concentration area: Photonics.

Advisor: Prof. Dr. Marcos Tavares de Melo.

Recife

2023

Catalogação na fonte
Bibliotecário Gabriel Luz, CRB-4 / 2222

C337f Cavalcanti Filho, Pedro Henrique Bezerra.
Frequency discriminators based on Sierpinski curve fractal FSS for 4-bit IFM systems using balanced binary code / Pedro Henrique Bezerra Cavalcanti Filho, 2023.
74 f.: il.

Orientador: Prof. Dr. Marcos Tavares de Melo.
Tese (Doutorado) – Universidade Federal de Pernambuco. CTG. Programa de Pós-Graduação em Engenharia Elétrica. Recife, 2023.
Inclui referências.
Textos em inglês.

1. Engenharia elétrica. 2. Código binário balanceado. 3. Curva de Sierpinski. 4. Medição instantânea de frequência. 5. Superfícies seletivas em frequência. I. Melo, Marcos Tavares de (Orientador). II. Título.

UFPE

621.3 CDD (22. ed.) BCTG / 2023 - 279

PEDRO HENRIQUE BEZERRA CAVALCANTI FILHO

# FREQUENCY DISCRIMINATORS BASED ON SIERPINSKI CURVE FRACTAL FSS FOR 4-BIT IFM SYSTEMS USING BALANCED BINARY CODE

Thesis presented to the Graduate Program in Electrical Engineering at the Federal University of Pernambuco, Technology and Geosciences Centre, as a partial requirement for obtaining the title of Doctor in Electrical Engineering. Concentration area: Photonics.

Approved: 14/08/2023.

**EXAMINING BOARD**

_____

Prof. Dr. Leandro Tiago Manera (External Examiner)
Universidade Estadual de Campinas

_____

Prof. Dr. Alexandre Jean René Serres (External Examiner)
Universidade Federal de Campina Grande

_____

Prof. Dr. Alfrêdo Gomes Neto (External Examiner)
Instituto Federal da Paraíba

_____

Prof. Dr. Francisco Ariaildo da Costa Sa Lucena (External Examiner)
Instituto Federal de Pernambuco

I dedicate this work to my grandmother Minervina (*in memorian*), for always supporting me throughout this long journey, and for providing me with all the necessary support to make its completion possible.

## ACKNOWLEDGEMENTS

There are many thanks to be given, but I can't help but start with God. However, this force that governs the universe manifests itself, it allowed me to come this far, and this combination of factors together allowed my desire for discovery to take shape.

I thank my parents Pedro and Jaqueline, as every day I see more and more how important the figure of parents is in shaping a human being, from believing in their offspring to the unconditional love that moves mountains to provide the best for them, and in this sense my parents represent the utmost for me in every way.

I thank my sister Priscilla for always being a loving and present sister in every moment of my life, along with my brother-in-law Welder, who is like a brother to me, and my nephew Pedro Lucas, who has just arrived in the family to bring joy to all of us.

I also thank my partner Cristiana for always being by my side, representing the person I love as my life partner, and with whom I want to spend the rest of my days.

I thank my grandmother Maria Helena for being my greatest example of resilience; my grandfather Euclides for planting the seed of science in my life since childhood; my grandfather Severino for being an example of how to live my days on this earth, and finally, my grandmother Minervina, who is not here physically to witness this achievement that she was so present for, but I know that wherever she is, she is proud to have been part of this process with so much love and care.

I thank my cousins, especially Havana, João, Johannes, and Mariana, for growing up with me like siblings.

I also thank my uncles for all the support and for being like second parents to me.

I thank my friends from adolescence who closely accompanied every phase of this process, including Fábio, João Pedro, Leonardo, Lucyano, Maurício, Murilo, Rodolfo, Wellisson, José Osmar, and others that I may not remember at the moment.

I thank my friends from undergrad, who were part of this long journey, including Ary, Elis, Jorge, Lyanderson and Válbio.

I thank my friends from postgrad, with whom we formed close bonds on this journey, including Alves, Bruno, Coutinho, Crislane, Douglas, Elias, Francisco, Gabriel, Giordano, Hawson, Manuelle, Tulio, and others that I may not remember at the moment.

I thank my advisor Marcos Tavares for believing in my ideas and giving me complete creative freedom in my research, as well as all the support I needed to come this far.

I also thank my advisor Raquel for introducing me to the world of microwaves and for being the most compassionate mentor I have ever known to this day.

And finally, I thank my brothers and sisters in arms, who supported me so much in this final phase, including Deisielly, Diego, Eva, Jéssica, Maurício, Patrick, Silene, Stefany, Veloso, and many others.

“You have power over your mind - not outside events. Realize this, and you will find strength.” (ANTONINUS, 161-180 B.C.).

## ABSTRACT

An Instantaneous Frequency Measurement (IFM) system consists of a set of elements capable of processing an input signal using discriminators to identify the sub-band to which the signal's frequency belongs. The displayed results are represented by binary values that reflect the output power of the discriminators. Therefore, it is of utmost importance to appropriately select the frequency response of these elements to ensure the proper functioning of the system. By designing the discriminators correctly, direct scanning can be achieved, eliminating the need for post-processing. In this thesis, evidence is presented that choosing a balanced binary code (BBC) to represent the output bits brings significant advantages in the design of frequency discriminators. The designed discriminators are composed of a set of four dual-band Frequency Selective Surfaces (FSS) based on the fractal geometry Sierpinski Curve, with different iterations, thus replacing traditional frequency discriminators such as interferometers and filters. As an application of the designed discriminators, a 4-bit IFM system will be hypothesized with a design resolution of 323.12 MHz for each of the 16 sub-bands distributed in the frequency range between 0.39 GHz and 5.56 GHz. The results of the computational simulations carried out in the CST Microwave Studio, along with the measurements using a network analyzer, were presented and compared, showing good correspondence. Both in measurements and in simulations, the FSS is placed between the antennas. The parameter analyzed in the simulations and measurements is the transmission coefficient, $S_{21}$, between two horn-type antennas used in the measurements and represented by ports 1 and 2 in the computational simulations.



Keywords: balanced binary code; instantaneous frequency measurement; Sierpinski curve; frequency selective surfaces.

## RESUMO

Um sistema de medição instantânea de frequência (IFM) consiste em um conjunto de elementos capazes de processar um sinal de entrada por meio de discriminadores, a fim de identificar a subfaixa a qual a frequência do sinal pertence. Os resultados exibidos são representados por valores binários que refletem a potência de saída dos discriminadores. Portanto, é de suma importância selecionar adequadamente a resposta em frequência desses elementos para garantir o funcionamento adequado do sistema. Ao projetar os discriminadores corretamente, é possível realizar a varredura diretamente, eliminando a necessidade de pós-processamento. Nesta tese, são apresentadas evidências de que a escolha de um código binário balanceado (BBC) para representar os bits de saída traz vantagens significativas no projeto dos discriminadores de frequência. Os discriminadores projetados são compostos por um conjunto de quatro superfícies seletivas de frequência (FSS) *dual-band* baseadas na geometria fractal Curva de Sierpinski, com diferentes iterações, substituindo assim os discriminadores de frequência tradicionais, como os interferômetros e filtros. Como aplicação dos discriminadores projetados, será conjecturado um sistema IMF de 4 bits com uma resolução de projeto de 323,12 MHz para cada uma das 16 sub-bandas distribuídas na faixa de frequência entre 0,39 GHz e 5,56 GHz Os resultados das simulações computacionais realizadas no CST Microwave Studio, juntamente com as medições utilizando um analisador de rede, foram apresentados e comparados, apresentando boa correspondência. Tanto nas medições, como nas simulações, a FSS é colocada entre as antenas. O parâmetro analisado nas simulações e medições é o coeficiente de transmissão, $S_{21}$, entre duas antenas tipo corneta utilizadas nas medições e representadas pelas portas 1 e 2 nas simulações computacionais.



Palavras-chave: código binário balanceado; curva de Sierpinski; medição instantânea de frequência; superfícies seletivas em frequência.

## LIST OF ILLUSTRATIONS


Figure 1 - (a) Modeling of a transmission line. (b) Modeling of an infinitesimal segment (Δz) of a transmission line. ..... 20
Figure 2 - Transmission line terminated in a load $ZL$. ..... 22
Figure 3 - Representation of a two-port network using S parameters. ..... 23
Figure 4 - Direction of vibration and propagation of a transverse wave. ..... 24
Figure 5 - Polarization ellipse. ..... 25
Figure 6 - Linear, vertical polarization. ..... 25
Figure 7 - Linear, horizontal polarization. ..... 26
Figure 8 - Circular Polarization. Left hand (blue) and Right hand (red) ..... 27
Figure 9 - (a) Aperture type FSS (b) Frequency response. ..... 33
Figure 10 - (a) Patch type FSS (b) Frequency response. ..... 33
Figure 11 - Examples of group 1: n-poles connected by the center. a) Dipoles, b) Tripoles, c) Anchor element, d) Cross of Jerusalem, e) Spiral square. ..... 35
Figure 12 - Examples of group 2: Loops. a) Four-legged loaded elements, b) Three-legged loaded elements, c) Circular loops, d) Square loops, e) Hexagonal loops. ..... 35
Figure 13 - Examples from Group 3: Solid interior. a) Solid square, b) Solid hexagon, c) Solid circle ..... 36
Figure 14 - Group 4: Combinations. ..... 36
Figure 15 - Step 1 of Sierpinski Curve Fractal Construction ..... 38
Figure 16 - The following six iterations of the Sierpinski Curve Fractal ..... 38
Figure 17 - Simple Frequency Discriminator IFM architecture ..... 43
Figure 18 - Proposed Frequency Discriminator IFM architecture ..... 44
Figure 19 - Frequency responses of a set of FSS based on the 4-bit traditional Gray-code .. 45
Figure 20 - Frequency responses of a set of FSS based on the 4-bit balanced Gray-code .... 46
Figure 21 - Geometry of the unit cells for the proposed FSS. (a) FSS1. (b) FSS2. (c) FSS3. (d) FSS4 ..... 47
Figure 22 - Photograph of the manufactured FSS. (a) FSS1. (b) FSS2. (c) FSS3. (d) FSS4. 48
Figure 23 - Image of the "Mesh View" function in the CST software active. ..... 49
Figure 24 - Simulated result for FSS 1. ..... 51
Figure 25 - Simulated result for FSS 2. ..... 52
Figure 26 - Simulated result for FSS 3. ..... 52
Figure 27 - Simulated result for FSS 4. ..... 53

Figure 28 - Bandwidths associated with the sub-bands for the simulated proposed IFM system. 54
Figure 29 - Sketch of the system for measurements of the FSS 55
Figure 30 - Experimental measurement of FSS 1 using a vector network analyzer. 56
Figure 31 - Comparison between the measured and simulated results of FSS 1. 56
Figure 32 - Comparison between the measured and simulated results of FSS 2. 57
Figure 33 - Comparison between the measured and simulated results of FSS 3. 57
Figure 34 - Comparison between the measured and simulated results of FSS 4. 58
Figure 35 - Bandwidths associated with the sub-bands for the simulated proposed IFM - measured 60
Figure 36 - Comparison between the measured results for the X and Y polarization for FSS 1. 62
Figure 37 - Comparison between the measured results for the X and Y polarization for FSS 2. 63
Figure 38 - Comparison between the measured results for the X and Y polarization for FSS 3. 63
Figure 39 - Comparison between the measured results for the X and Y polarization for FSS 4 64
Figure 40 - Meteor 1500 CLP05 antenna. 65
Figure 41 - Correspondence between ZDR values and the size of a raindrop. 66

## LIST OF TABLES


Table 1 - Correspondence between traditional and reflected decimal representations. ..... 29

Table 2 - Correspondence between binary and decimal representations (RBC and BBC)..... 30

Table 3 - Comparison between IFM main proprieties. ..... 42

Table 4 - Frequency ranges and their corresponding logic levels for FSS 1. ..... 50

Table 5 - Frequency ranges and their corresponding logic levels for FSS 2 ..... 50

Table 6 - Frequency ranges and their corresponding logic levels for FSS 3 ..... 50

Table 7 - Frequency ranges and their corresponding logic levels for FSS 4 ..... 51

Table 8 - Identified sub-bands and digital words of the four proposed FSS obtained from the simulated results. ..... 53

Table 9 - Frequency ranges and their corresponding logic levels for FSS 1 - Measured. ..... 59

Table 10 - Frequency ranges and their corresponding logic levels for FSS 2 - Measured. ..... 59

Table 11 - Frequency ranges and their corresponding logic levels for FSS 3 - Measured. ..... 59

Table 12 - Frequency ranges and their corresponding logic levels for FSS 4 - Measured. ..... 59

Table 13 - Digital Words of the four proposed FSS obtained from the measured results. ..... 60

Table 14 - Transition Frequencies and Power levels - FSS 1..... 61

Table 15 - Transition Frequencies and Power levels - FSS 2..... 61

Table 16 - Transition Frequencies and Power levels - FSS 3..... 61

Table 17 - Transition Frequencies and Power levels - FSS 4..... 61

## LIST OF ABBREVIATIONS

| | |
|---|---|
| A/D | Analogic To Digital |
| BBC | Balanced Binary Code |
| BW | Bandwidth |
| C-DPR | Dual-Polarization C-Band Weather Radars |
| DFD | Digital Frequency Discriminator |
| FSS | Frequency Selective Surface |
| IFM | Instantaneous Frequency Measurement |
| LHCP | Left-Hand Circular Polarization |
| RBC | Reflected Binary Code |
| RF | Radio Frequency |
| RHCP | Right-Hand Circular Polarization |
| S-DPR | Dual-Polarization S-Band Weather Radars |
| TTL | Transistor–Transistor Logic |
| UWB | Ultra-Wideband |
| VNA | Vector Network Analyzer |
| ZDR | Differential Reflectivity |

## LIST OF SYMBOLS

| | |
|---|---|
| Γ | Reflection Coefficient |
| λ | Wavelength |
| c | Speed of Light |
| $\varepsilon_r$ | Dielectric Constant |
| $S_{ij}$ | Scattering Parameter |
| $V_{th}$ | Threshold Voltage |
| $Z_{in}$ | Input Impedance of a Transmission Line |
| $Z_0$ | Characteristic Impedance of a Transmission Line |
| $Z_L$ | Load Impedance |

**SUMMARY**


| | | |
|---|---|---|
| **1** | **INTRODUCTION** | **17** |
| **2** | **THEORICAL BASIS** | 19 |
| 2.1 | TRANSMISSION LINES | 19 |
| 2.2 | SCATTERING PARAMETERS IN MICROWAVE NETWORKS | 22 |
| 2.3 | WAVE POLARIZATION | 24 |
| **2.3.1** | **Linear polarization** | **25** |
| 2.3.1.1 | Vertical Polarization | 25 |
| 2.3.1.2 | Horizontal Polarization | 26 |
| **2.3.2** | **Circular polarization** | **26** |
| 2.4 | REFLECTED BINARY CODE (GRAY CODE) | 27 |
| 2.5 | BALANCED BINARY CODE (BALANCED GRAY CODE) | 29 |
| **3** | **FREQUENCY SELECTIVE SURFACES** | 32 |
| 3.1 | FSS CLASSIFICATION | 32 |
| **3.1.1** | **Fill** | **33** |
| **3.1.2** | **Shielding Material Thickness** | **33** |
| **3.1.3** | **Geometry** | **34** |
| 3.1.3.1 | Fractal Geometry | 36 |
| **4** | **INSTANTANEOUS FREQUENCY MEASUREMENT** | 39 |
| 4.1 | STRUCTURE OF A DIGITAL FREQUENCY DISCRIMINATOR (DFD) | 42 |
| 4.2 | SIMPLE FREQUENCY DISCRIMINATOR | 42 |
| 4.3 | PROPOSED DISCRIMINATOR | 44 |
| 4.4 | FREQUENCY RESPONSES FOR FSS DISCRIMINATORS IN IFM SYSTEM | 45 |
| **5** | **DESIGN AND FABRICATION OF THE FSS** | 47 |
| **6** | **ANALYSIS OF SIMULATED AND MEASURED RESULTS** | 49 |
| 6.1 | SIMULATION RESULTS | 49 |
| 6.2 | EXPERIMENTAL SETUP FOR MEASUREMENTS | 54 |
| 6.3 | EXPERIMENTAL RESULTS | 56 |
| **7** | **POSSIBLE APPLICATION FOR THE DESIGNED DISCRIMINATORS** | 65 |

7.1 DUAL-POLARIZATION (POLARIMETRIC) RADARS ..... 65
**8 CONCLUSION** ..... 67
8.1 SUGESTION FOR FUTURE WORK..... 68
**9 SCIENTIFIC PRODUCTION..... 68**
**REFERENCES**..... 70

# 1 INTRODUCTION

IFM (Instantaneous Frequency Measurement) systems are electronic devices used to perform real-time frequency measurements without the need for subsequent digital processing. These systems are essential in applications that require high precision and speed in frequency measurement, such as radar systems, communications, navigation, target recognition, and other military applications [1].

One advantage of using Frequency Selective Surfaces (FSS) as frequency discriminators in IFM systems is the ability to select specific frequencies in an input signal [2]. FSS are composed of a set of sub-wavelength metallic elements designed to reflect or transmit electromagnetic waves at specific frequencies. This allows FSS to be used to filter radio signals and select only the frequencies of interest for measurement [3].

Furthermore, the use of a balanced binary code, which will be detailed later, can enhance an IFM system utilizing Frequency Selective Surfaces as frequency discriminators by reducing the number of elements needed to fabricate the devices. This code allows efficient optimization of FSS elements, maximizing selectivity and minimizing signal loss [4], [5], [6].

In addition, the symmetries present in fractal geometries can be used to create FSS that exhibit a similar response for different wave polarizations, making these devices more versatile and useful in a wide range of applications. Fractal geometries offer advantages such as the ability to reduce the size and weight of devices, as well as improve electromagnetic efficiency [7]. Fractal geometries exhibit self-similarity properties that allow reproduction at multiple scales, which can be used to design FSS across a wide range of frequencies [8].

These features make IFM systems with FSS frequency discriminators and fractal geometries highly useful in applications that require efficient and precise real-time frequency measurements, especially in military applications.

The proposed doctoral thesis aims to develop and optimize frequency discriminators based on dual-band frequency selective surfaces for IFM systems. The research will focus on exploring the advantages of using FSS as frequency discriminators, including their ability to operate over a wide frequency range, compactness, and ease of fabrication. The performance of the FSS-based discriminators will be evaluated through simulations and experiments, considering factors such as bandwidth and insertion loss. The proposed FSS-based discriminators have potential applications in various fields such as radar systems, wireless communication, and electronic warfare. The research aims to contribute to the development of

more efficient and compact frequency discriminators for IFM systems, with the potential for significant impact in both civilian and military applications.

The FSS were modeled through computer simulations, fabricated in the laboratory using microwave substrates, and measured at the IFPB Campus João Pessoa Microwave Laboratory. The measured and simulated results obtained were appropriately compared.

This work is organized into 8 chapters.

Chapter 2 provides the necessary theoretical foundation for understanding the work, encompassing basic concepts of transmission lines, scattering parameters in microwave networks, and wave polarization. Next, both the traditional and balanced gray binary codes are introduced.

In Chapter 3, the concept and main classifications of frequency selective surfaces (FSS) are presented, including the use of fractal geometries, specifically the Sierpinski curve geometry.

Chapter 4 discusses the instantaneous frequency measurement (IFM) systems, starting from the structure of digital frequency discriminators to an outline of the behavior of the discriminators that will be presented in this work.

Chapter 5 focuses on the design and fabrication of the designed FSS.

Chapter 6 analyzes and compares the simulated and measured results, describing the setup and measurement process of the system parameters.

Chapter 7 mentions a possible application of the conjectured system based on its characteristics.

Chapter 8 deals with the conclusions of this thesis.

# 2 THEORICAL BASIS

In this section, fundamental basic concepts will be presented to aid in understanding the project. Brief explanations will be given on both transmission line analysis and microwave network analysis. Additionally, an overview of the balanced gray binary code, which served as the foundation for the frequency discriminator design in the project, will also be provided. Additionally, the important concept of wave polarization will be presented, focusing on linear wave polarizations.

## 2.1 TRANSMISSION LINES

Transmission lines are structures that convey electromagnetic energy in a guided manner from one point to another in a circuit. Examples of simple transmission lines include two parallel wires, coaxial cable, and microstrip lines [9]. A transmission line, in the transverse electromagnetic (TEM) propagation mode, is represented by at least two parallel wires as shown in Figure 1(a), where voltages and currents can vary in magnitude and phase along its length [10]. A longitudinal segment of an infinitesimal length $\Delta z$ of a transmission line can be modeled by discrete elements, as depicted in Figure 1(b).

Capacitance and inductance are the elements that represent the storage of electrical and magnetic energy, respectively, while resistors represent circuit losses [11]. Specifically, the parallel capacitor and series inductor represent the capacitance and self-inductance between the two conductor wires, respectively. The series resistor accounts for losses in the conductors, while the parallel resistor represents losses associated with the dielectric material. We will use the formulation based on reference [10] for transmission lines.

The discrete elements R, L, G, and C have specific roles in electrical systems. The element R represents the series resistance per unit length for both conductor wires, while the element L denotes the series inductance per unit length for both conductor wires. Additionally, the element G refers to the parallel conductance per unit length for both conductor wires, and the element C is related to the parallel capacitance per unit length for both conductor wires. These elements play essential roles in the study and design of electrical circuits and systems, each with distinct characteristics and specific impacts on the behavior of components and the overall network.

Figure 1 - (a) Modeling of a transmission line. (b) Modeling of an infinitesimal segment (Δz) of a transmission line

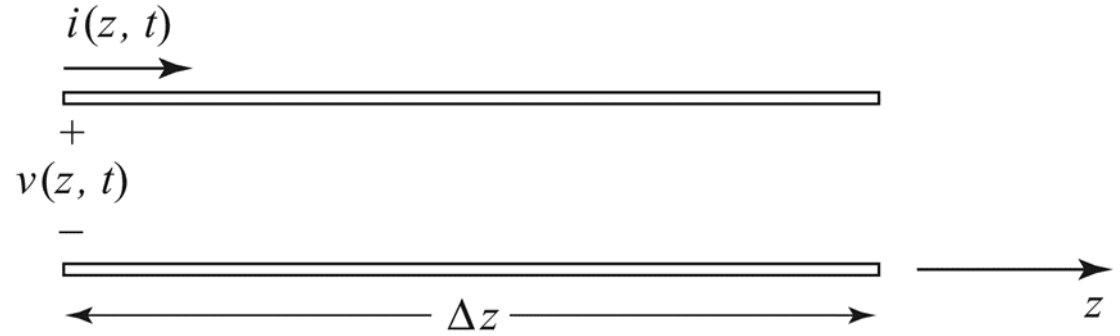


(a)

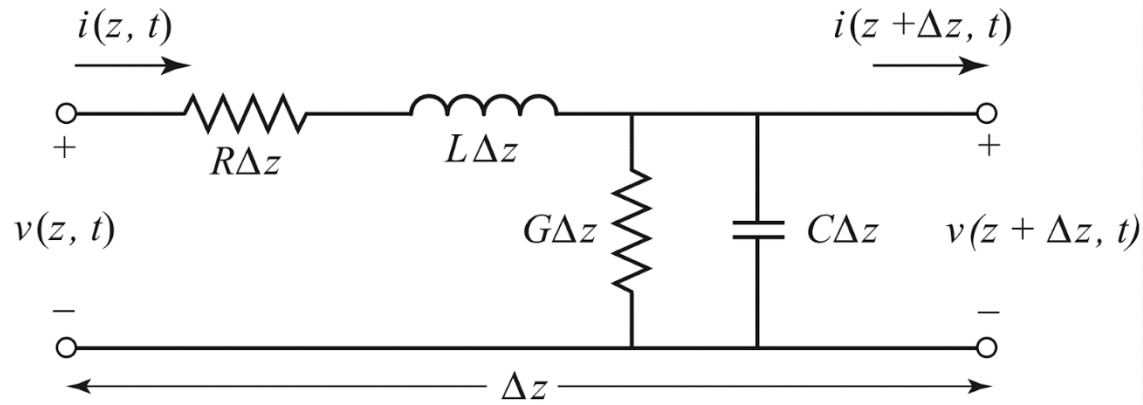


(b)

Source: [10]

Applying the Kirchhoff's laws of voltage and current in the circuit of Figure 1 (b), we have respectively:

$$v(z,t) - R\Delta z i(z,t) - L\Delta z \frac{\partial i(z,t)}{\partial t} - v(z+\Delta z,t) = 0 \quad (1)$$

$$i(z,t) - G\Delta z v(z+\Delta z,t) - C\Delta z \frac{\partial v(z+\Delta z,t)}{\partial t} - i(z+\Delta z,t) = 0 \quad (2)$$

After some algebraic operations on Equations (1) and (2) and assuming the sinusoidal harmonic regime for voltage and current, we have:

$$\frac{d^2V(z)}{dz^2} - \gamma^2 V(z) = 0 \quad (3)$$

$$\frac{d^2I(z)}{dz^2} - \gamma^2 I(z) = 0 \quad (4)$$

The term γ is the complex propagation constant, and $Z_0$ is the characteristic impedance of the line, given by:

$$\gamma = \alpha + j\beta = \sqrt{(R + j\omega L)(G + j\omega C)} \tag{5}$$

$$Z_0 = \frac{R+j\omega L}{\gamma} = \sqrt{\frac{R+j\omega L}{G+j\omega C}} \tag{6}$$

And the wavelength and phase velocity are given by:

$$\lambda = \frac{2\pi}{\beta} \tag{7}$$

$$v_p = \frac{\omega}{\beta} = \lambda f \tag{8}$$

For the scenario in which the losses of the transmission line are negligible, α=0 with R=0 and G=0, equations (3), (4), (5), (6), (7), and (8) transform accordingly:

$$V(z) = V_o^+ e^{-\gamma z} + V_o^- e^{\gamma z} \tag{9}$$

$$I(z) = I_o^+ e^{-\gamma z} + I_o^- e^{\gamma z} \tag{10}$$

$$\gamma = \alpha + j\beta = j\omega\sqrt{LC} \tag{11}$$

$$Z_0 = \sqrt{\frac{L}{C}} \tag{12}$$

$$\lambda = \frac{2\pi}{\beta} = \frac{2\pi}{\omega\sqrt{LC}} \tag{13}$$

$$v_p = \frac{\omega}{\beta} = \frac{1}{\sqrt{LC}} \tag{14}$$

The relationship between current and voltage in an infinite transmission line is equal to its characteristic impedance $Z_0$. When this line is terminated by a load $Z_L$ different from $Z_0$

(Figure 2), the relationship between voltage and current at the load is $Z_L$, thus, a reflected wave occurs to satisfy this condition at z = 0. The relationship between the amplitude of the reflected voltage and the incident voltage at this point is defined as the reflection coefficient, Γ.

$$\Gamma = \frac{V^-_0}{V^+_0} = \frac{Z_L - Z_0}{Z_L + Z_0} \tag{15}$$

The impedance seen at a distance *l* from the load can be obtained through equations (9), (10), and (15):

$$Z_{in} = Z_0 \frac{Z_L + jZ_0 \tan(\beta l)}{Z_0 + jZ_L \tan(\beta l)} \tag{16}$$

Figure 2 - Transmission line terminated in a load $Z_L$

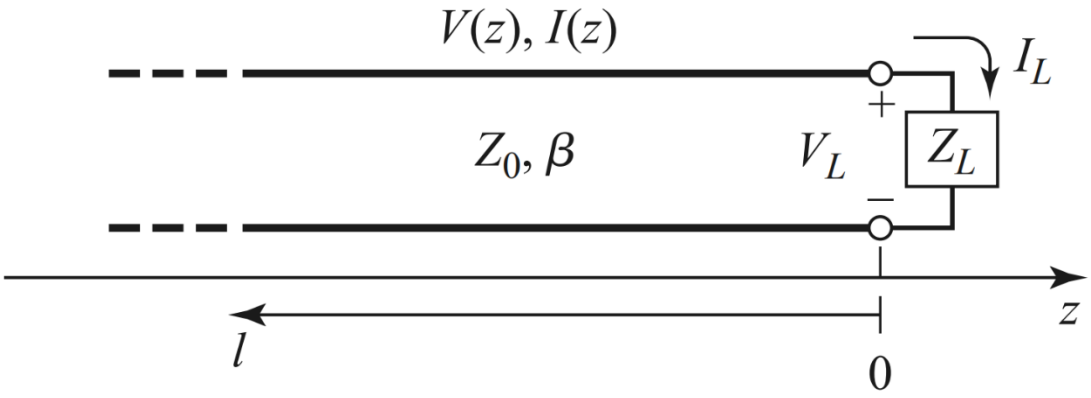


Source: [10]

## 2.2 SCATTERING PARAMETERS IN MICROWAVE NETWORKS

The scattering parameters are typically presented in matrix form. They quantify the RF signal propagation through a multi-port network [12]. The scattering parameter matrix for an N-port network, which contains $n^2$ coefficients, is shown in equations (17) and (18).

$$\begin{bmatrix} V_1^- \\ V_2^- \end{bmatrix} = \begin{bmatrix} S_{11} & S_{12} \\ S_{21} & S_{22} \end{bmatrix} \cdot \begin{bmatrix} V_1^+ \\ V_2^+ \end{bmatrix} \tag{17}$$

$$[V^-] = [S] \cdot [V^+] \tag{18}$$

Where,

$[V^-]$ is the matrix of reflected voltages at each port,

$[V^+]$ is the matrix of incident voltages at each port, and

[S] is the scattering matrix, also known as the S matrix.

To better understand the circuit analysis using S parameters, Figure 3 illustrates a two-port network along with all the signal paths captured by S-parameters expressed by (17).

Figure 3 - Representation of a two-port network using S parameters

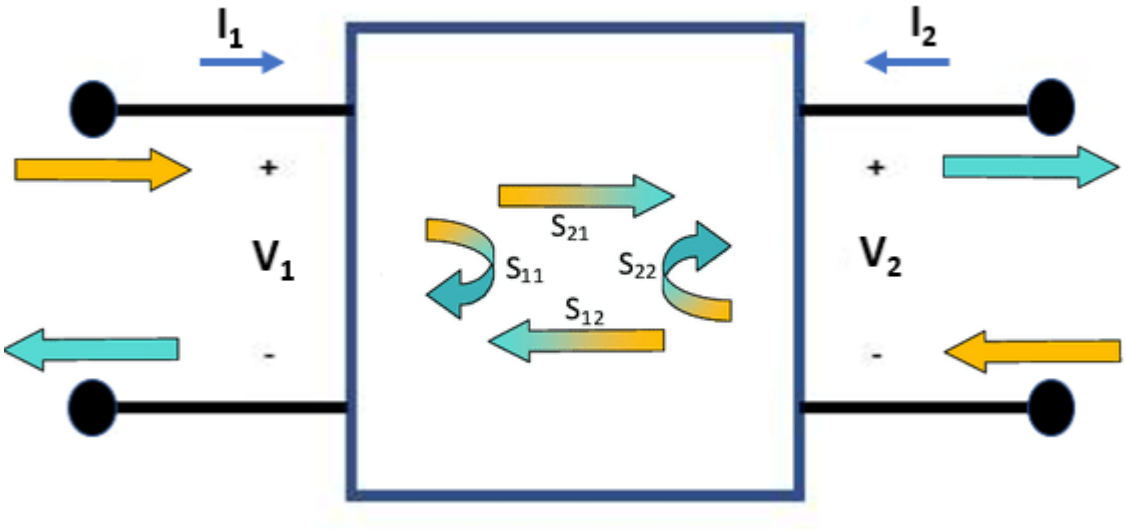


Source: Modified from [13]

More specifically, each element of the matrix is given by:

$$S_{ij} = \left.\frac{V_i^-}{V_j^+}\right|_{V_k^+=0,\text{ to } k\neq j} \tag{19}$$

Since the S parameters are generally complex, it is more convenient to represent them in terms of magnitude and phase, that is:

$$S_{ij} = |S_{ij}|e^{j\phi_{ij}} \tag{20}$$

To utilize amplitude in decibels (dB), one uses:

$$|S_{ij}|(dB) = 20\log|S_{ij}| \tag{21}$$

For the characterization of filters, it is necessary to define two additional parameters: insertion loss between ports *i* and j, where $i \neq j$, meaning it is always measured from one port to another, and return loss at port j, always measured relative to the same port.

## 2.3 WAVE POLARIZATION

To understand an important contribution of this research in relation to previously developed ones, the concept of wave polarization is crucial. In the following topic, we will briefly explain the necessary concepts within the scope of this work.

Wave polarization is a unique characteristic of transverse waves, where the direction of vibration is perpendicular to the direction of propagation, according to Figure 4.

Figure 4 - Direction of vibration and propagation of a transverse wave

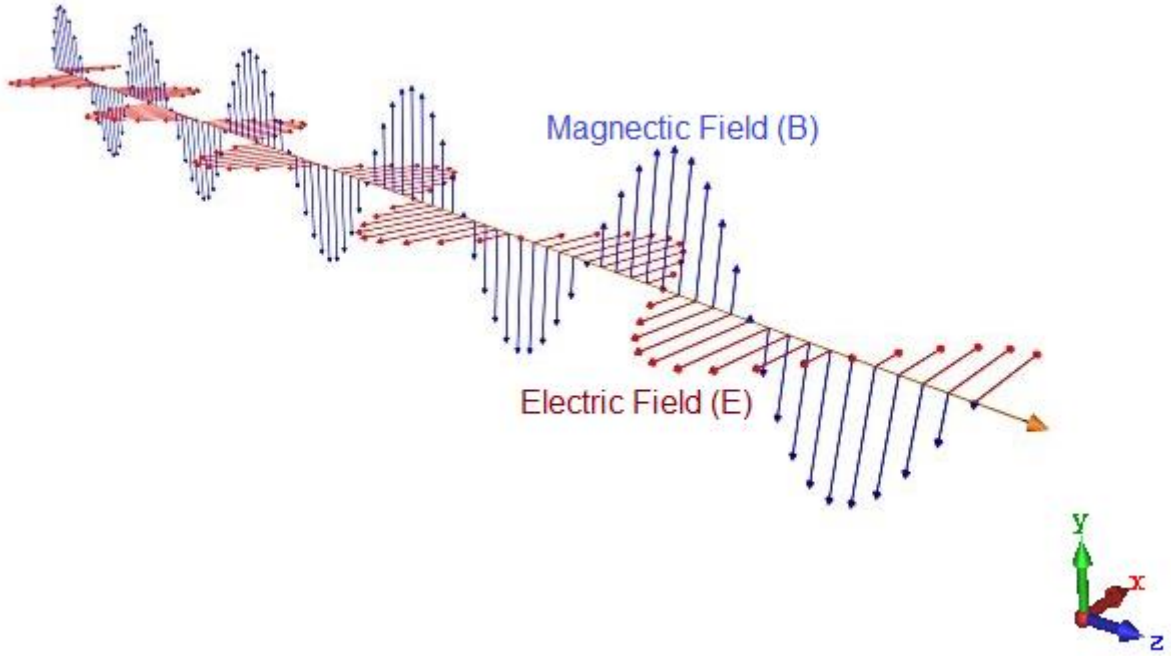


Source: Modified from [14].

By convention, the polarization of an electromagnetic wave is associated with the direction of vibration of the electric field vector [15]. Let the electric field of a wave propagating in the +z direction be:

$$\vec{E}(z,t) = E_1 \cos(\omega t - \beta z)\vec{i} + E_2 \cos(\omega t - \beta z + \phi)\vec{j} = E_x\vec{i} + E_y\vec{j} \quad (22)$$

In the most general case, as the wave propagates, the tip of the electric field vector describes an inclined ellipse in the *xy* plane. In other words, considering the wavefront, as the wave propagates, the shape of the ellipse depends on $E_1$, $E_2$, and the phase angle between the horizontal and vertical components, according to Figure 5.

Figure 5 - Polarization ellipse

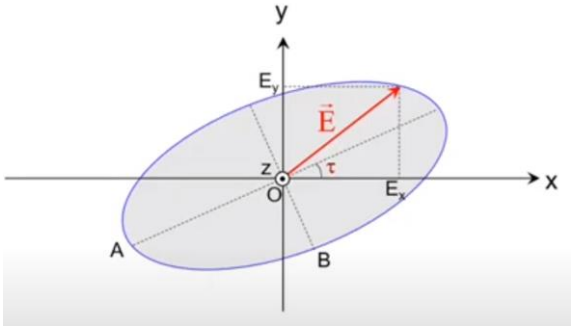


Source: Modified from [16].

### 2.3.1 Linear polarization

In linear polarization, the electric field vector always points in the same direction as the wave propagates. There are two main types of linear polarization: vertical and horizontal [17].

#### 2.3.1.1 Vertical Polarization

Vertical polarization occurs when the electric field is vertical, and the horizontal component of the electric field is zero ($E_1$= 0), E = $E_y$. Figure 6 shows an example of vertically polarized wave transmission, consisting of a feed horn on a parabolic reflector.

Figure 6 - Linear, vertical polarization

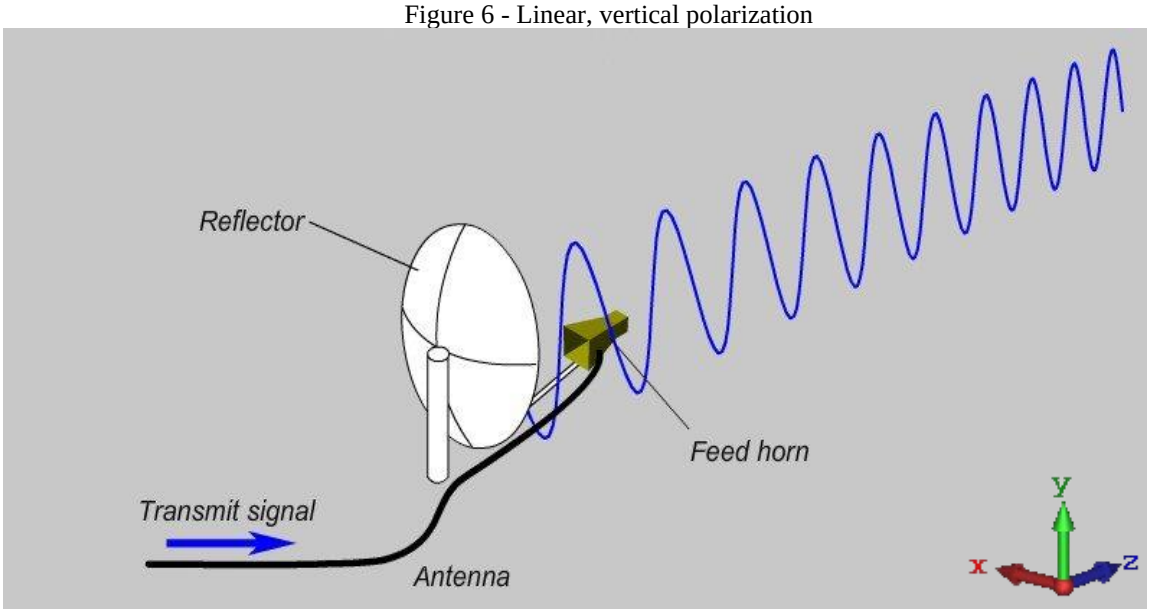


Source: Modified from [14].

#### 2.3.1.2 Horizontal Polarization

Horizontal polarization occurs when the electric field is horizontal, and the vertical component of the electric field is zero ($E_2 = 0$), E = $E_x$. Figure 7 shows an example of horizontally polarized wave transmission, also consisting of a feed horn on a parabolic reflector.

Figure 7 - Linear, horizontal polarization.

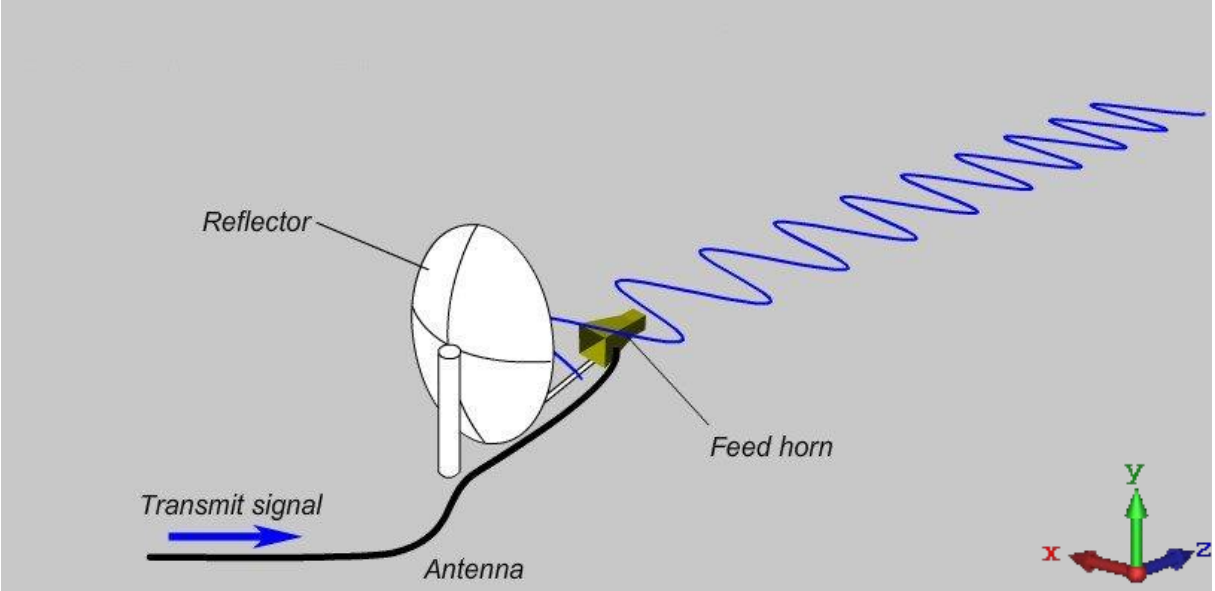


Source: Modified from [14].

### 2.3.2 Circular polarization

In Circular polarization, the electric field vector rotates in a circle in the *xy* plane as the wave propagates. In order to have circular polarization, two conditions must be simultaneously satisfied:

1. The magnitudes of the electric field components in the x and y directions must be equal.
2. There must be a phase difference of 90 degrees (or π/2 radians) between the *x* and *y* components of the electric field.

There are two types of circular polarization: right-hand circular polarization (RHCP) and left-hand circular polarization (LHCP) [18].

In right-hand circular polarization, the phase difference between the horizontal and vertical components is -90 degrees. This polarization is represented by the acronym RHCP because, by pointing the thumb of the right hand in the direction of wave propagation, the electric field rotates in the direction of the fingers of the right hand.

In contrast, in left-hand circular polarization, the phase difference between the horizontal and vertical components is +90 degrees. This polarization is represented by the acronym LHCP, and by pointing the thumb of the left hand in the direction of wave propagation, the electric field rotates in the direction of the fingers of the left hand.

Figure 8 shows an example of an application of circular polarization. The feed system hardware of the uplink station can be designed to make the wave spin in either a counter-clockwise direction (LHCP - left-hand circular polarization) or a clockwise direction (RHCP - right-hand circular polarization).

Figure 8 - Circular Polarization. Left hand (blue) and Right hand (red)

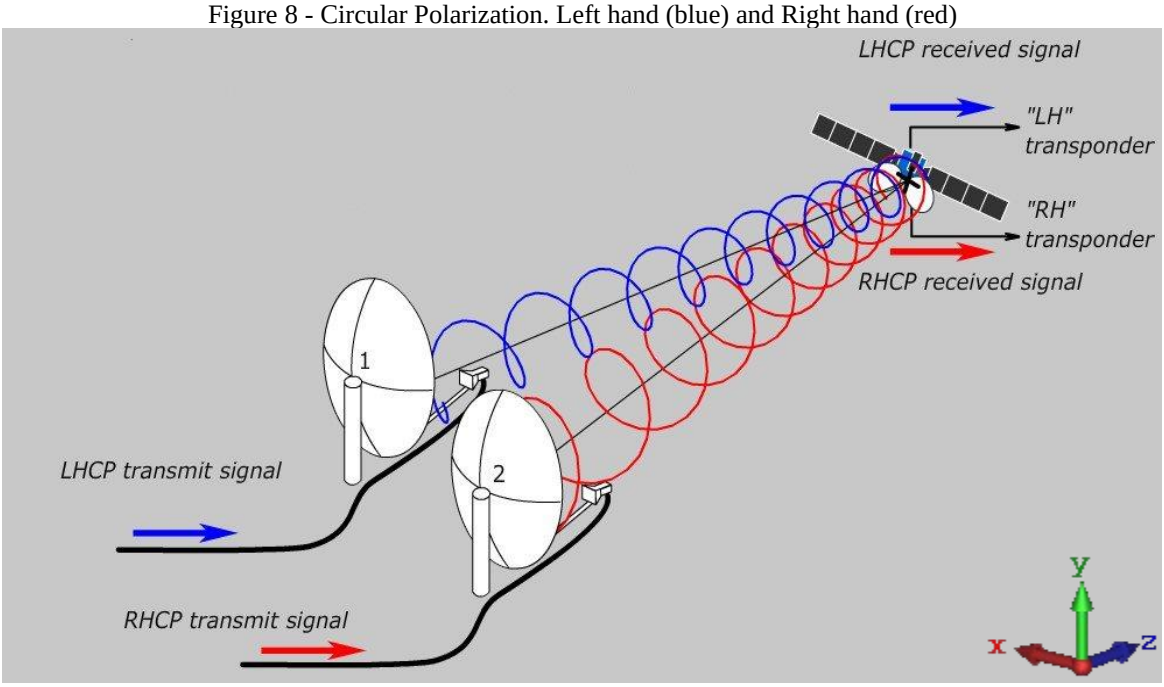


Source: Modified from [14].

## 2.4 REFLECTED BINARY CODE (GRAY CODE)

In digital systems, information is stored and transmitted using binary representation, which means using numerical representation in base two, as opposed to decimal representation [19]. This practice stems from the ease of representing these quantities in electronic systems, with the bits 0 and 1 being taken as absence or presence of a signal, respectively.

For example, Transistor-Transistor Logic (TTL) assumes that the bit 0 will be represented by a voltage level of zero, and the bit 1 by a voltage level of five volts [20].

With the ability to store *n* bits, it is possible to describe $2^n$ different states, which can be used to represent $2^n$ distinct instances of information. Each possible set of n bits is called a

binary word. From this principle arises the need to create a correspondence between decimal and binary representations.

The most direct way to achieve this correspondence is to establish a mathematical relationship between binary algebra and decimal algebra, as explained below.

$$A_{10} = \sum_{n=0}^{N} b_n \cdot 2^n \tag{23}$$

where $A_{10}$ represents the decimal representation of a number and $b_n$ represents the binary digits (and hence, the bits) of the binary representation of the same number. In Table 1, the relationship between the traditional binary representation and the decimal representation for the first 16 natural numbers is exemplified. Naturally, both sets can be arbitrarily ordered. Some orderings will have advantages over others. The main and obvious advantage of using the traditional binary representation is the ease of conversion between representations.

However, other representations emerge to address operational problems, such as fixed-point and floating-point representations (which can represent a finite subset of real numbers) and the two's complement representation (which facilitates algebraic operations at the machine level).

For our study, we are interested in a specific phenomenon: transitions between binary words. By observing Table 1, it is possible to see that, in the traditional binary code, there are transitions of more than one bit between some consecutive words. As will be seen later, these transitions will be represented by cutoff frequencies in reject-band filters.

Thus, in a transition where more than one bit is simultaneously altered, two or more filters must have the same cutoff frequency. Despite having advanced filter design and manufacturing techniques, frequency shifts still occur between the expected and measured values. One way to avoid the occurrence of this phenomenon is to replace the code used to represent the output bits with a code in which there is no simultaneous transition of bits between consecutive words.

Table 1 - Correspondence between traditional and reflected decimal representations.

| Decimal representation | Traditional binary representation | Reflected binary representation |
|---|---|---|
| 0 | 0000 | 0000 |
| 1 | 0001 | 0001 |
| 2 | 0010 | 0011 |
| 3 | 0011 | 0010 |
| 4 | 0100 | 0110 |
| 5 | 0101 | 0111 |
| 6 | 0110 | 0101 |
| 7 | 0111 | 0100 |
| 8 | 1000 | 1100 |
| 9 | 1001 | 1101 |
| 10 | 1010 | 1111 |
| 11 | 1011 | 1110 |
| 12 | 1100 | 1010 |
| 13 | 1101 | 1011 |
| 14 | 1110 | 1001 |
| 15 | 1111 | 1000 |

Source: The author.

Gray code, named after its inventor Frank Gray, or Reflected Binary Code (RBC) is a possible form of representation. It is called "reflected" due to the reflection of the code itself. This code allows for the creation of a set of words in which there is no simultaneous transition between consecutive words. Table 1 presents the set of words generated by the RBC for four bits. In the following sections, the use of reflected binary code in the creation of frequency discriminators will be discussed, as they are fundamental devices for IFM.

## 2.5 BALANCED BINARY CODE (BALANCED GRAY CODE)

An alternative to depict binary words is the Balanced Binary Code. This representation emerges from the need to standardize the number of transitions for each binary digit. This is particularly crucial in electromechanical systems, where the longevity relies directly on the count of internal component switches. If the utilized representation code features balanced transitions, the individual lifespan of each component will be comparable.

To highlight this fact, it's worth noting that the least significant bit of the representation in Balanced Binary Code undergoes eight transitions when traversing the 16 words, whereas the most significant bit transitions only once.

The solution to this issue lies in selecting a word order that, while maintaining the property of having only one transition per consecutive word, ensures an equal total number of transitions per binary digit in each column. This representation is referred to as Balanced Binary Code (BBC), and a 4-bit instance is displayed in Table 2.

Table 2 - Correspondence between binary and decimal representations (RBC and BBC)

| Decimal Representation | Reflected Binary Representation | Balanced Binary Representation |
|---|---|---|
| 0 | 0000 | 0000 |
| 1 | 0001 | 1000 |
| 2 | 0011 | 1100 |
| 3 | 0010 | 1101 |
| 4 | 0110 | 1111 |
| 5 | 0111 | 1110 |
| 6 | 0101 | 1010 |
| 7 | 0100 | 0010 |
| 8 | 1100 | 0110 |
| 9 | 1101 | 0100 |
| 10 | 1111 | 0101 |
| 11 | 1110 | 0111 |
| 12 | 1010 | 0011 |
| 13 | 1011 | 1011 |
| 14 | 1001 | 1001 |
| 15 | 1000 | 0001 |

Source: The author.

It can be observed that in BBC, regardless of their position, each binary digit experiences four transitions. Furthermore, the spacing between transitions is more uniform.

The reader should note that the least significant bit encounters four transitions when considering the code in a circular manner. For this bit, the fourth transition occurs when the code increments from the last word, returning to the beginning.

In the upcoming sections, we will discuss a method for creating frequency discriminators based on these codes. Moreover, it will be demonstrated that by utilizing these

codes, not only the decoding process is simplified but also the FSS design, compared to traditional solutions for creating DIFMs.

# 3 FREQUENCY SELECTIVE SURFACES

Frequency selective surfaces are periodic structures composed of repetitive geometric patterns designed to exhibit filtering properties in relation to the incidence of electromagnetic waves at different frequencies [21],[22]. These surfaces are widely explored in the field of microwave engineering and antennas, offering a range of functionalities such as spectral filtering, selective absorption, polarization selectivity, and radiation directionality [23].

The main application of FSS is related to their filtering capability, allowing for the efficient control and manipulation of electromagnetic signals at various frequencies. They can be used as key components in passive filter designs, such as bandpass filters, rejection filters, pass filters, and narrowband filters [21], [22]. These filters are essential for the selectivity and efficiency of wireless communication systems, enabling the transmission and reception of signals in different frequency channels simultaneously.

Furthermore, fractal geometries have been incorporated into FSS design, providing a significant advantage in terms of performance and miniaturization characteristics. Space-filling curves [24], based on fractal concepts, have been widely explored in the optimization and design of FSS. They offer the ability to achieve enhanced performance, such as wide bandwidth, lower insertion loss, and more selective filtering responses, while reducing the structural complexity and physical size of the devices.

These innovations in the use of fractal geometries in FSS design have contributed to the development of miniaturized high-performance electromagnetic and electrostatic devices [25], [26],[27]. In applications such as wireless communication devices, sensors, antennas, and integrated circuits, miniaturization plays a crucial role in system efficiency, power consumption, and space savings. The incorporation of space-filling curves based on fractal geometries in FSS allows for the creation of compact and efficient devices, meeting the growing demands for advanced electromagnetic and electrostatic electronic systems.

## 3.1 FSS CLASSIFICATION

FSS can be classified in different ways. In this chapter, some of their classifications are presented.

### 3.1.1 Fill

As we can see in Figure 9, the FSS with aperture-type elements acts as a bandpass filter. In other words, as the elements resonate, the structure gradually becomes invisible to the incident wave. It is only at the resonance frequency of the FSS that the total transmission of the wave occurs. However, the FSS with conducting elements functions as a stopband filter, as shown in Figure 10. The elements resonate and, as a result, radiate the incident power in the direction of reflection. At the resonance frequency of the structure, it behaves as a perfect conductor, reflecting the incident wave completely [28].

Figure 9 - (a) Aperture type FSS (b) Frequency response

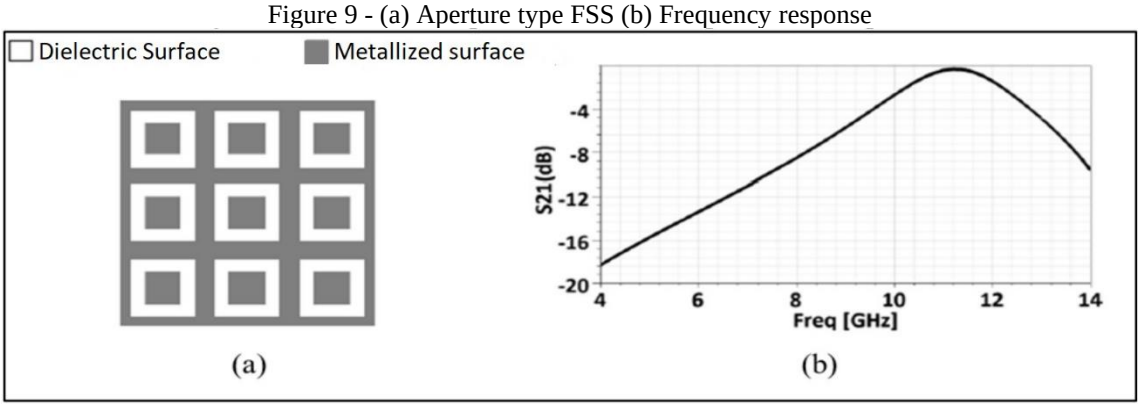


Source: [29]

Figure 10 - (a) Patch type FSS (b) Frequency response

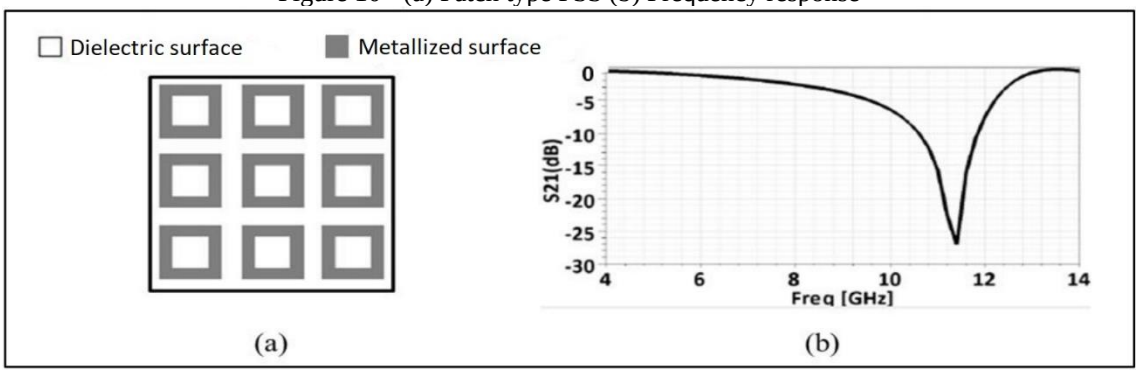


Source: [29]

### 3.1.2 Shielding Material Thickness

FSS can still be categorized as thin shield or thick shield, depending on the thickness of the component. Thin shield FSS typically refers to a shield with printed circuit elements that have a thickness less than $0.001\lambda_0$, where $\lambda_0$ represents the wavelength corresponding to the

resonant frequency of the shield. Generally, thin shield FSS are lightweight, compact, and can be produced at a low cost using traditional printed circuit manufacturing technologies, as used in this study. Conversely, thick shield FSS is heavy and its production necessitates precise handling of a thick metal block. Overlapped waveguides have been a popular form of thick shield FSS. The advantage of thick shield FSS is that the ratio of transmitted frequency to reflected frequency can be reduced, which is suitable for communication satellite antennas operating in multiple frequency bands [30].

### 3.1.3 Geometry

The selection of the appropriate element can be crucial when designing a band-pass or band-stop FSS. Certain elements possess inherent characteristics that make them either more wide-ranging or more limited in their bandwidth, whereas others can be extensively modified through design [21].

According to [21], elements can be organized into four groups:

Group I: The center connected or N-poles,

Group 2: The loop types such as the three- and four-legged loaded elements; the circular loops; and the square and hexagonal loops, exemplified in Figure 12;

Group 3: Solid interior or plate types of various shapes, Figure 13; and

Group 4: Combinations, exemplified in Figure 14.

Elements from Group 1 can be seen in Figure 11, the most common forms are: narrow dipole [30], Jerusalem cross [31] and crossed dipole [32].

Figure 11 - Examples of group 1: n-poles connected by the center. a) Dipoles, b) Jerusalem cross, c) Crossed dipoles

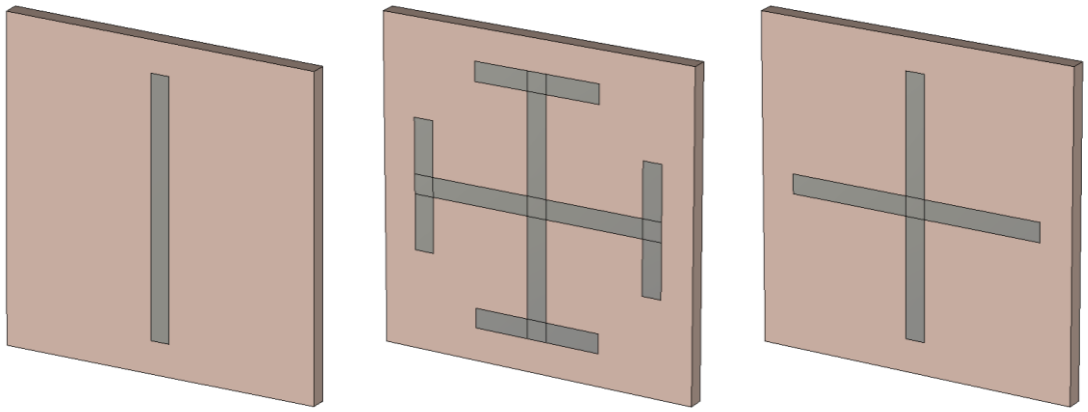

Source: The author.

The elements of spiral or loop types constitute Group 2. The prevalent types include: square loops [33], double square loops [34], squares arranged in a grid [35], and concentric circular bands [36]. The spire type elements are depicted in Figure 12.

Figure 12 - Examples of group 2: Loops. a) Square loops, b) Double square loops, c) Squares arranged in a grid, d) Concentrical circular bands

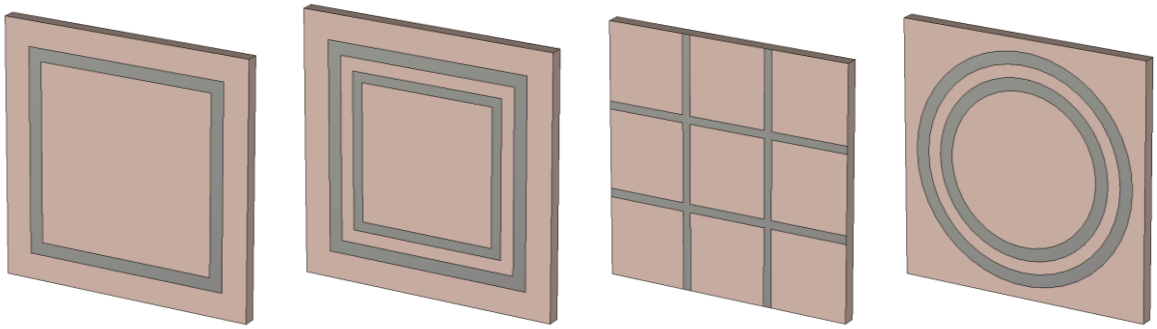

Source: The author.

Group 3 is formed by various shapes of solid interior or plate types. The most common types are: rectangular [30] hexagonal [29] and circular patches [37]. Elements of this group can be seen in Figure 13.

Figure 13 - Examples from Group 3: Solid interior. a) Rectangular, b) Hexagonal, c) Circular patches

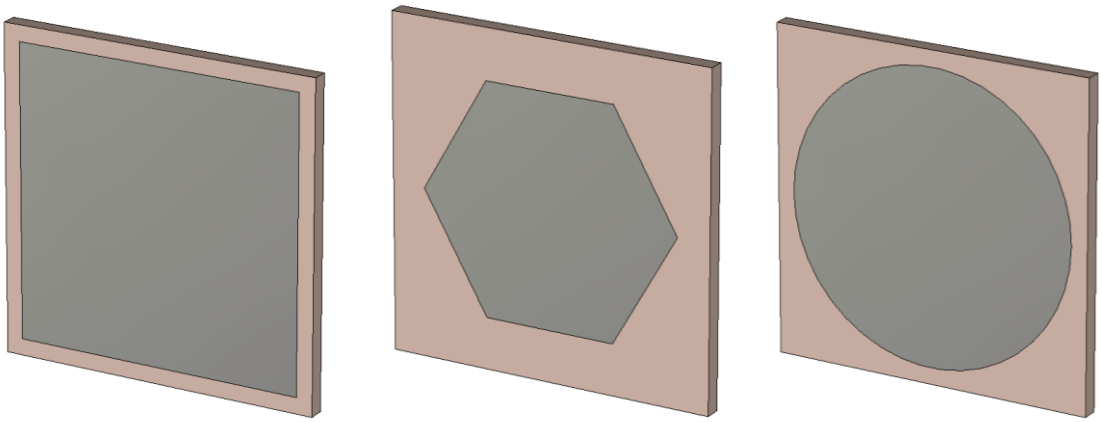

Source: The author.

Group 4 is the elements formed from a combination of typical elements. An example of combination can be seen in Figure 14.

Figure 14 - Group 4: Combinations

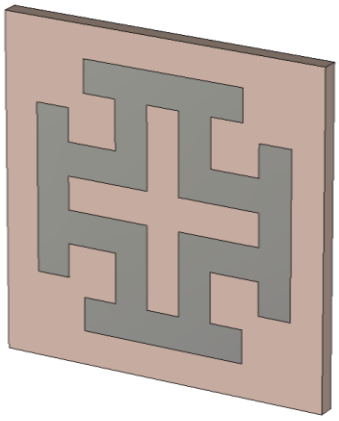

Source: The author.

### 3.1.3.1 Fractal Geometry

Fractal geometry is a branch of mathematics that studies complex and irregular geometric structures in which individual parts resemble the whole at different scales. These geometries exhibit remarkable properties such as self-similarity, geometric complexity, and self-filling. Thus, fractal geometry describes certain phenomena of nature or intricate objects, where Euclidean geometry (points, lines and circles) is not able to describe, due to the simplicity of its forms [38].

Self-similarity is a fundamental characteristic of fractal geometries, where a figure repeats itself at different scales. This means that when zooming in on a part of the structure, a similar shape to the original figure can be observed. The self-similarity at various scales allows,

for example, the creation of FSS that are capable of operating over a wide range of frequencies, making it possible to manipulate electromagnetic waves at different wavelengths. This property of fractal structures also allows to obtain performance similar to that of larger structures in a reduced space. This is especially important in applications where size and weight are limited, such as antennas and communication devices.

Geometric complexity is another property of fractals. Unlike traditional geometric shapes such as circles, squares, or triangles, fractals have infinite complexity. Even if a part of a fractal is magnified, new details and patterns emerge, resulting in a structure that becomes increasingly complex and intricate. Equally important, self-filling, or space-filling, is a unique feature of a group of fractals. These geometries occupy a finite amount of space while completely filling the available space. For example, a fractal curve may have a fractional dimension, such as 1.58, which means that it fills space more efficiently than a straight line (dimension 1) or a plane (dimension 2).

The Sierpinski curve, discovered by the Polish mathematician Wacław Sierpiński, is an example of a curve with these properties. Therefore, because the Sierpiński curve is space-filling, its Hausdorff dimension (in the limit $n \to 0$) is 2 [39]. The algorithm for forming this geometry consists of the following steps:

Step 1: Consider an imaginary square with sides of length *l* divided into 4 equal triangles. Ordering the adjacent triangles in a clockwise direction, oriented by the center of the square, connect the barycenters (or incenters) of these triangles in the given order, as shown in Figure 15.

Step 2: Now, consider that each triangle generated in the previous step is divided into two isosceles triangles. Once again, connect the barycenters (or incenters), passing through all the triangles created by these subdivisions, ordered in a clockwise direction, oriented by the center of the square.

This process is repeated indefinitely to obtain the Sierpinski Curve Fractal. Therefore, Figure 16 represents iterations 2, 3, 4, 5, 6, and 7, respectively. The steps are not dependent on each other; they only depend on the triangles generated in the iterations $2^{k+1}$ subtriangles are generated in iteration k). The total length ($l_n$) of the curve for each iteration is given by equation (24). Note that the initial points were not connected to the final points to facilitate understanding.

$$l_n = \frac{2}{3}\left(1+\sqrt{2}\right)2^n - \frac{1}{3}\left(2-\sqrt{2}\right)\frac{1}{2^n} \quad (24)$$

Figure 15 - Step 1 of Sierpinski Curve Fractal Construction

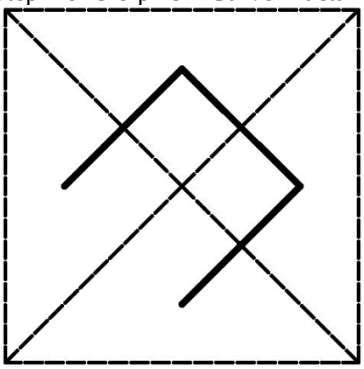

Source: The author.

Figure 16 - The following six iterations of the Sierpinski Curve Fractal

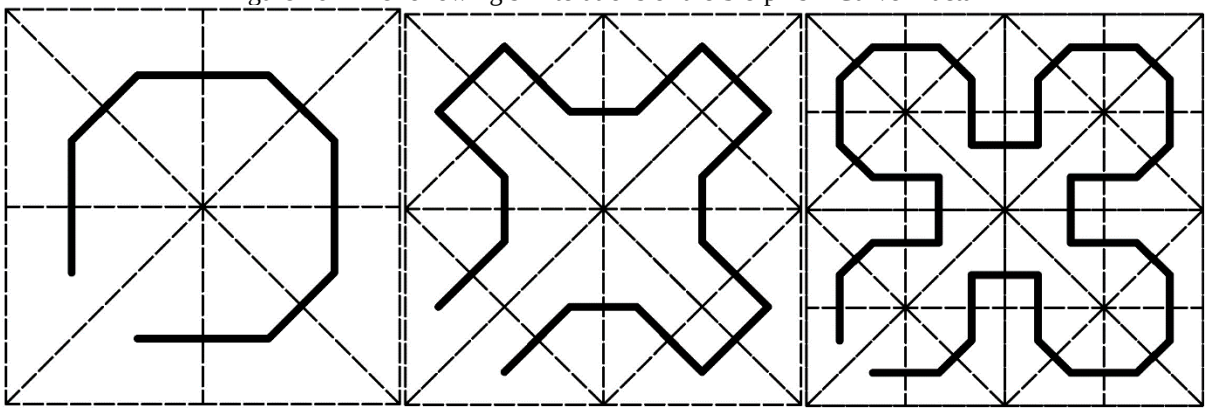

Iteration 2 Iteration 3 Iteration 4

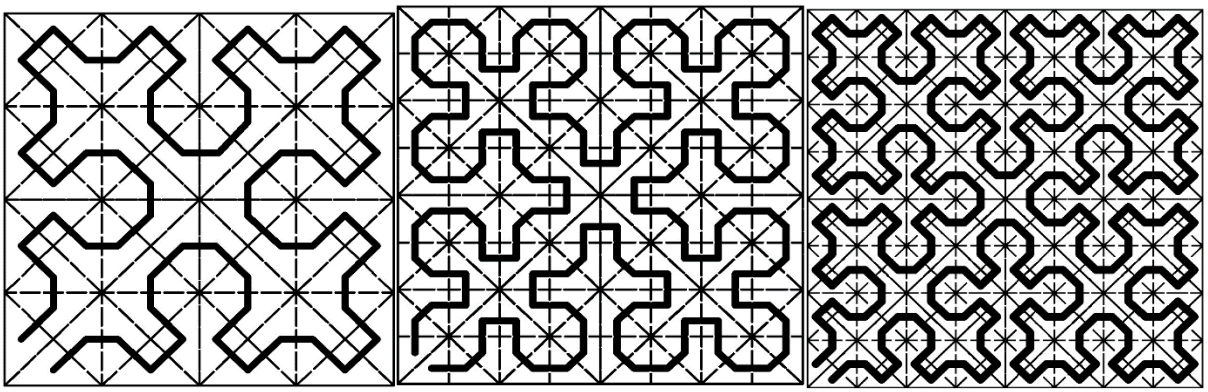

Iteration 5 Iteration 6 Iteration 7

Source: The author.

# 4 INSTANTANEOUS FREQUENCY MEASUREMENT

Instantaneous Frequency Measurement (IFM) systems play an important role in various applications, ranging from wireless communications to radar and surveillance systems. These systems are designed to instantly and accurately measure and analyze the frequency of radio or microwave signals.

The development of IFM systems dates back to the 1950s and 1960s when the rapid detection and analysis of radio signals became crucial for military purposes. Initially, these systems were used to detect enemy radar signals and determine their frequencies, enabling quick identification and classification. With technological advancements, IFM systems evolved and found applications in a wide range of civilian and military fields [40].

A critical component in IFM systems is the frequency discriminator circuit, responsible for measuring the instantaneous frequency of the input signal [41]. These circuits convert the frequency into a proportional voltage, allowing for further analysis and processing by other system components.

There are two main types of frequency discriminators: analog and digital. Analog frequency discriminators use components such as inductors, capacitors, and operational amplifiers to measure the instantaneous frequency of the input signal. They operate in the analog domain and provide a continuous voltage proportional to the input signal's frequency. These circuits are widely used in real-time applications where a quick response is required.

On the other hand, digital frequency discriminators convert the input signal into a digital representation before performing frequency analysis. These systems utilize digital signal processing techniques to measure the frequency. The input signals are sampled and digitally processed, allowing for higher accuracy and flexibility in signal processing. Digital frequency discriminators are extensively used in modern systems where digital processing is preferred due to its higher processing capability and ease of implementation.

IFM systems have various practical applications. For instance, they are used in radio receivers to measure the instantaneous frequency of received signals, enabling proper tuning of the receiver in wireless communications. In radar systems, IFM systems are employed to measure the frequency of return signals, facilitating accurate detection and tracking of targets. Moreover, IFM systems are utilized in spectrum analyzers to measure and display the frequency spectrum of a signal, proving useful in signal monitoring and analysis applications, such as identifying interferences or planning frequencies in communication networks. They can also be

employed in surveillance systems to monitor and analyze radio or microwave signals in a specific area.

Research of significant relevance in the utilization of microwave devices as frequency discriminators has been conducted in [42], [43], and [44], where coplanar interferometers were innovatively employed for application in IFM systems. However, the physical characteristics of interferometers introduce certain drawbacks for their practical use. Due to their composition, which includes at least one splitter, one combiner, and two delay lines, tuning them to the center frequency results in waveform irregularities when wide frequency bands are observed. Additionally, the adjustment of transition frequencies and the slope of the $S_{21}$ curve is solely determined by the difference in electrical length between the delay lines, which limits the system to the simultaneous tuning of these parameters. Moreover, there is a lack of extensive literature on miniaturization techniques concerning conventional interferometers.

Given the limitations of the aforementioned interferometers, researchers have explored the use of filters as frequency discriminators for IFM systems in [42] and [45]-[50]. These filters, being free from the need for splitters or delay lines, allow for individual adjustment of transition frequencies and slope characteristics around those frequencies. Furthermore, there exists a broad range of literature regarding filter miniaturization techniques. Additionally, in conjunction with the application of filters as discriminators in IFM systems, the utilization of balanced binary code decoding has been implemented in their design. This approach ensures an equal number of transitions for each bit and guarantees that each filter possesses the same number of sub-bands. These design considerations enhance system efficiency and reduce its overall size.

References [42] and [43] present frequency discriminators based on delay lines. However, due to the physical limitations of these delay lines, increasing the resolution of systems requires enlarging their physical dimensions. In [43], an alternative approach is proposed to mitigate this issue by utilizing the Hilbert fractal curve. This curve exhibits the unique property of self-filling and enables the infinite expansion of its length while remaining confined within a finite area. Subsequently, in [51] and [44], PIN diodes were employed for selecting the delay lines, eliminating the need for additional devices for each bit of the system. However, the operational delay caused by diode switching represents a disadvantage. Consequently, in [52], the concept of delay lines and the usage of PIN diodes in conjunction with the Hilbert fractal curve were combined to design an even more compact frequency discriminator.

Lastly, an innovative application of FSS as frequency discriminators in IFM systems was developed in [2]. However, this system has inherent limitations as it associates its sub-bands with reflected binary codes, resulting in a halving of the rejected band width with the integration of each new FSS into the system. To enhance system resolution, an increasing number of FSS units with narrower sub-bands and a higher number of resonances must be added, making the design process more complex. Moreover, due to the utilization of reflected binary codes, transitions of more than one bit occur between certain consecutive words. Another aspect worth noting is the choice of geometry, which employed a simple dipole. While this geometry lacks novelty in the study of FSS, it also lacks symmetry in the *xy* plane, thereby limiting the device's performance to a specific wave polarization. Despite the aforementioned limitations, this research demonstrated innovation and exceptional relevance in employing FSS as frequency discriminators in IFM systems.

Therefore, the research conducted in [2] served as a catalyst for the research presented in this thesis, aiming to provide innovative contributions and address the aforementioned limitations. The objective is to explore the forefront of knowledge in this field. Table 3 provides a comprehensive overview of the primary advantages and disadvantages found in the state-of-the-art research on IFM systems utilizing microwave devices as frequency discriminators. The discriminators proposed in this work incorporate the Fractal Sierpinski Curve geometry in a novel manner, which not only integrates spatial characteristics such as self-filling but also enables IFM devices employing these discriminators to operate with dual polarization, a fundamental attribute for enhancing device versatility. Furthermore, the adoption of balanced binary code decoding offers various design advantages, including the equalization of the number of binary transitions, the dimensions of the discriminators, and the resonant frequencies of the FSS. These advantages are combined with the utilization of a low-cost dielectric substrate.

Table 3 - Comparison between IFM main proprieties.

| | Coplanar interferometers using RBC [42] | Multi-band reject filters using BBC [6] | Hilbert Fractal geometry interferometers using RBC [52] | Simple dipole FSS using RBC [2] | Sierpinski curve fractal geometry FSS using BBC (This Work) |
|---|---|---|---|---|---|
| Operation in Dual-polarization | yes | unknow | yes | no | yes |
| Freedom to adjust the transition frequencies | low | high | low | low | high |
| Homogeneous number of bit transitions | no | yes | no | no | yes |
| Miniaturization Techniques | low | average | high | low | high |
| Cost | high | low | average | low | low |
| Incidence angle dependence | no | no | no | yes | yes |

Source: The author.

## 4.1 STRUCTURE OF A DIGITAL FREQUENCY DISCRIMINATOR (DFD)

Conventional IFM receivers feature several circuits such as amplifier limiter, detectors, power dividers, discriminators, and analog-to-digital converters. The essential element of these systems is the frequency discriminators.

## 4.2 SIMPLE FREQUENCY DISCRIMINATOR

In Figure 17, we have a block diagram of an architecture for conventional IFM systems. In it, the circuits are divided into individual blocks, and an unknown signal is received at the system input. After going through the following stages, a digital signal is obtained at its output.

Figure 17 - Simple Frequency Discriminator IFM architecture

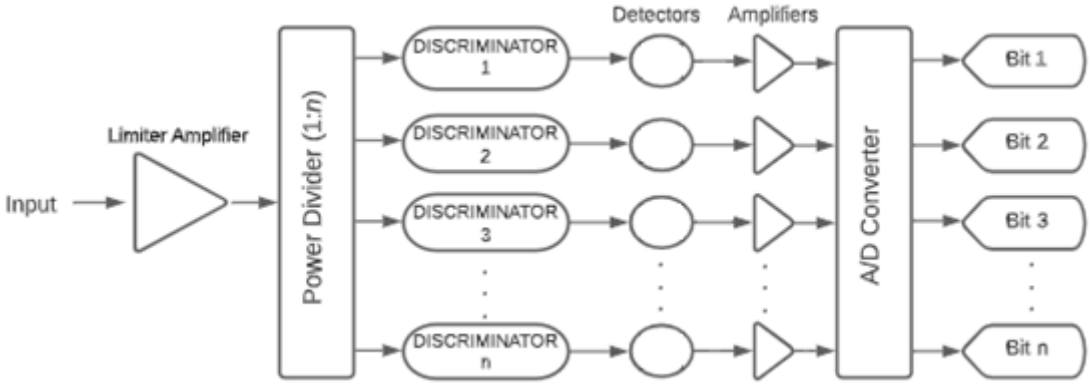


Source: The author.

The limiter amplifier is the primary component of the system, serving the purpose of selectively amplifying low-power RF signals with a good signal-to-noise ratio, functioning as a band-pass filter. Tuned to the system's operating band, this filter aims to provide a high gain to the signal, thereby enhancing the receiver's sensitivity and reducing the impact of simultaneously entering signals with frequencies different from those for which the device was designed. It should be noted that the input signal is unknown, as observed at the system's input.

Following the limiter amplifier, we have the power dividers, which equally divide the signal power from the limiter amplifier and transmit each generated signal to the frequency discriminators.

The subsequent stage, consisting of the discriminators, constitutes the primary element of the IFM and will be appropriately replaced in this study by the proposed FSS.

The second-to-last component of the system consists of the detectors, which are responsible for quadrature detection of these signals. It is at this stage that the system provides a DC voltage to the amplifiers and subsequently to the A/D converters, which is the final stage of the system. Ultimately, in the final stage, the power limit levels from the detectors are analyzed with a reference level ($V_{th}$), also referred as *Threshold*. This threshold/power level determines the logical level of each detector and, consequently, the frequency range in which the unknown input signal is located.

The logical level "0" will be represented when the detector's power is below the $V_{th}$, and the logical level "1" will be represented when the detector's power is above the $V_{th}$. In practice, the reference voltages in the discriminators do not need to be equal. A more detailed explanation of this topic will be discussed in subsequent chapters.

## 4.3 PROPOSED DISCRIMINATOR

An arrangement for frequency discriminators systems will be proposed in this work, using frequency selective surfaces, UWB antennas, and an analog-to-digital converter as main components, as can be observed in Figure 18.

Figure 18 - Proposed Frequency Discriminator IFM architecture

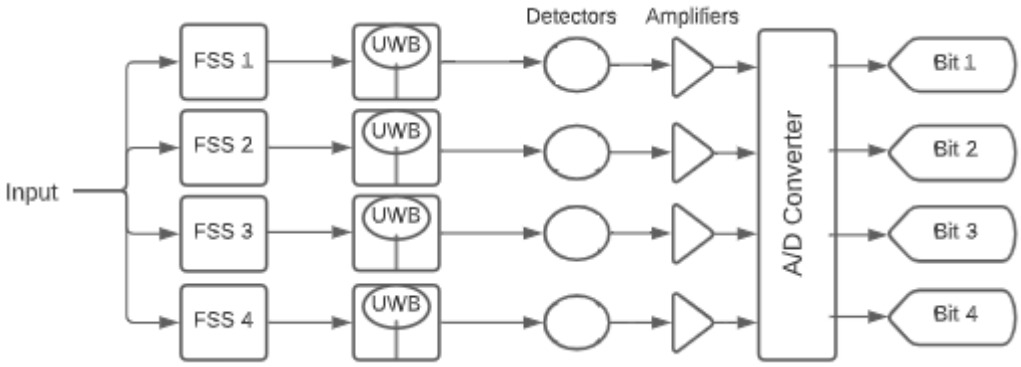


Source: The author.

To achieve digital conversion, multiple discriminators (1...n) must be placed in parallel, and a power limit level ($V_{th}$) is set for digital conversion. In the case of this work, four FSS will be placed in parallel to obtain the signal at the output of the A/D converter. Each FSS will be responsible for one bit of the 4-bit digital word at the system output. For a system with *N* bits with *N* FSS, we will have the ability to identify $2^n$ sub-bands within the design bandwidth.

The resolution frequency (f) is given by:

$$f = \frac{BW}{2^n} \ , \tag{25}$$

where ($BW = fmáx - fmín$) represents the bandwidth of the system.

In the case of the proposed system for this work, for the value of *f*, we will have: $BW$ ($= 5.56\ GHz - 0.39\ GHz = 5.17\ GHz$ and the value of $2^n$ will be equal to $2^4$ = 16, as explained earlier. Therefore, the design value for the system's resolution frequency will be equal to 5.17/16 = 323.12 MHz. However, the values of the frequency sub-bands obtained in the simulations and measurements showed shifts due to compressions in certain sub-bands.

## 4.4 FREQUENCY RESPONSES FOR FSS DISCRIMINATORS IN IFM SYSTEM

As an initial endeavor to substitute filters and interferometers with FSS, early designs used the discriminators frequency response to compose IFM systems. Consequently, the frequency responses of some FSS comprised several bands of rejection, as depicted in Figure 19.

In [2], FSS responses were implemented following the conventional Gray-code. The rejected bands of each FSS had a bandwidth that was half the bandwidth of the rejected bands of its predecessor. Nonetheless, difficulties may arise when attempting to construct FSS using this approach, mainly due to the significant variation in the rejected band's bandwidth. Constructing with the narrowest rejected bands within a single discriminator poses a challenge because it requires a considerable number of resonance frequencies, especially as the system resolution increases.

As previously mentioned, it is feasible to implement the frequency discriminator by utilizing various combinations of $2^n$ terms. In particular, the adoption of a balanced Gray-code ensures the avoidance of spurious outputs, as only one-bit changes at each sub-band transition. Furthermore, this choice guarantees that each FSS will possess an equal number of rejected bands, simplifying the design process. Consequently, the bands will exhibit less variation in fractional bandwidth.

A series of frequency selective surfaces based on the balanced Gray-code showcases the frequency response depicted in Figure 20. This selection facilitates the implementation of the FSS, and this type of system was adopted in this work, as illustrated in the subsequent sections.

Figure 19 - Frequency responses of a set of FSS based on the 4-bit traditional Gray-code

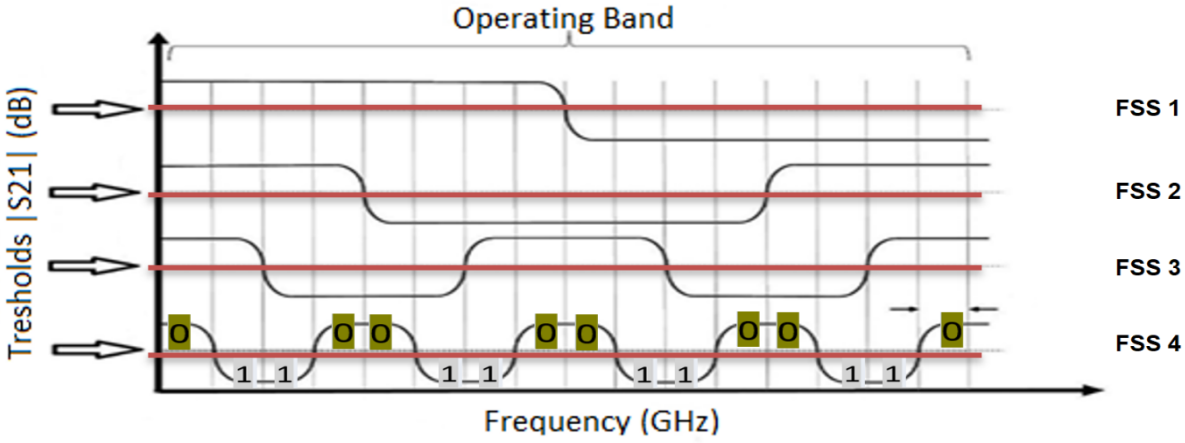


Source: Modified from [4].

Figure 20 - Frequency responses of a set of FSS based on the 4-bit balanced Gray-code

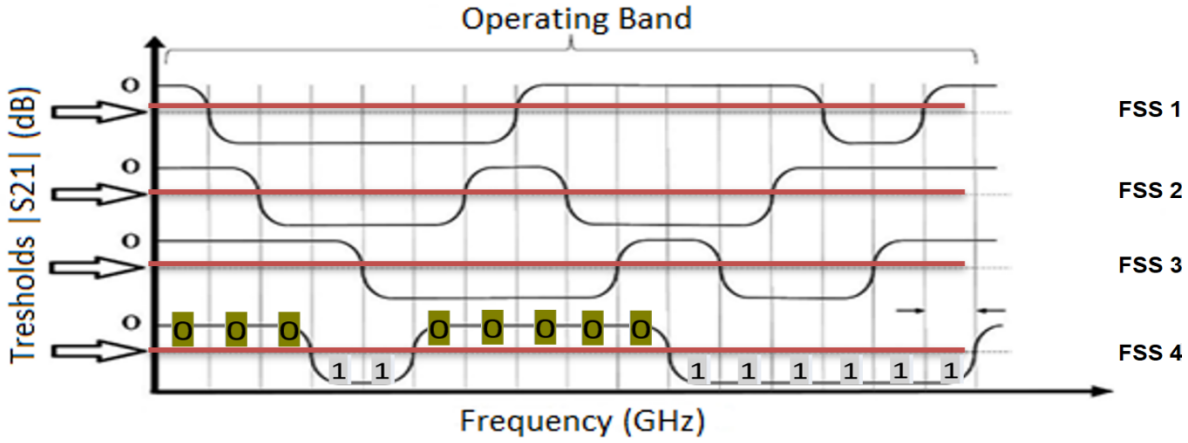


Source: Modified from [4].

# 5 DESIGN AND FABRICATION OF THE FSS

New FSS based on the Sierpinski Curve geometry, in addition to the one already published in [53], are proposed. The FSS differ in terms of the iterations of the geometry used, according to the formation law demonstrated in [54]. FSS 1 and FSS 3 were based on the fourth iteration of the Sierpinski Curve, while FSS 2 and FSS 4 were based on the fifth and seventh iterations, respectively. These geometries and dimensions were designed through simulations to form the binary words for each of the 16 subbands. The dimensions were adjusted to modify the corresponding parameters and provide the required resonance frequencies for the project. The system was designed to operate in the frequency range between 0.39 GHz and 5.56 GHz, with a bandwidth of 5.17 GHz.

Figure 21 presents the proposed unit cells for the four FSS (1-4) with their respective dimensions. As seen in previous chapters, these characteristics, as well as the chosen dielectric, will influence the resonance frequency value of the system. The FSS were printed on FR-4 substrate due to their good mechanical and electrical stability with low dielectric losses, in addition to being commercially available and cost-effective. The used model has a thickness of h = 1.6 mm, relative permittivity $\varepsilon_r$ = 4.3 and loss tangent tg δ = 0.025. The devices were fabricated at the Microwave Measurements Laboratory of GTEMA/IFPB (Federal Institute of Paraíba) using printed circuit techniques, through the adhesive fixation and etching with ferric chloride procedure, and were subsequently measured using a horn antenna arrangement. The dimensions of the FSS are 21 cm x 21 cm, determined by the measurement panel aperture (20 cm x 20 cm), and the fabricated FSS prototypes are shown in Figure 22.

Figure 21 - Geometry of the unit cells for the proposed FSS. (a) FSS1. (b) FSS2. (c) FSS3. (d) FSS4

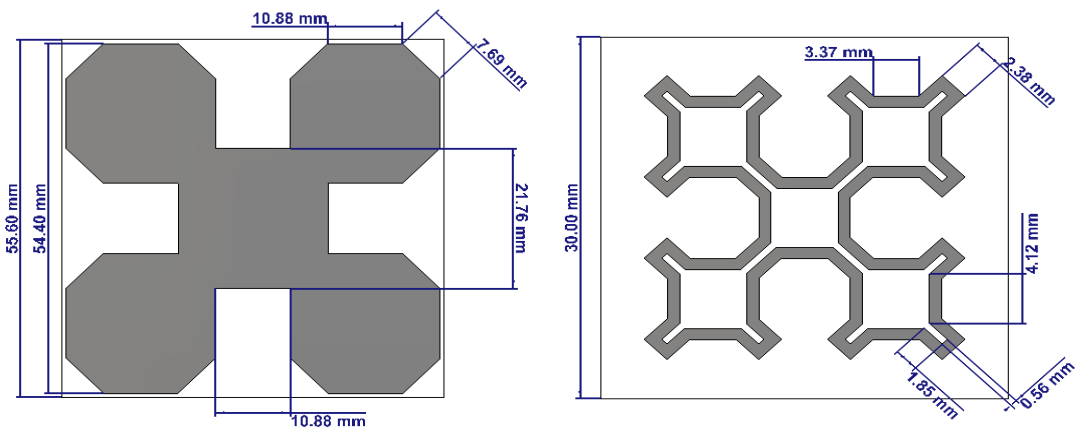


(a) (b)

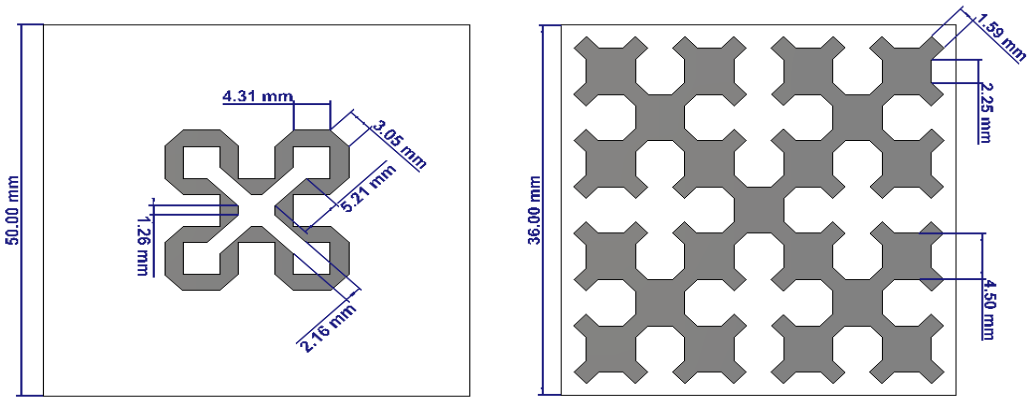


(c) (d)

Source: The author.

Figure 22 - Photograph of the manufactured FSS. (a) FSS1. (b) FSS2. (c) FSS3. (d) FSS4.

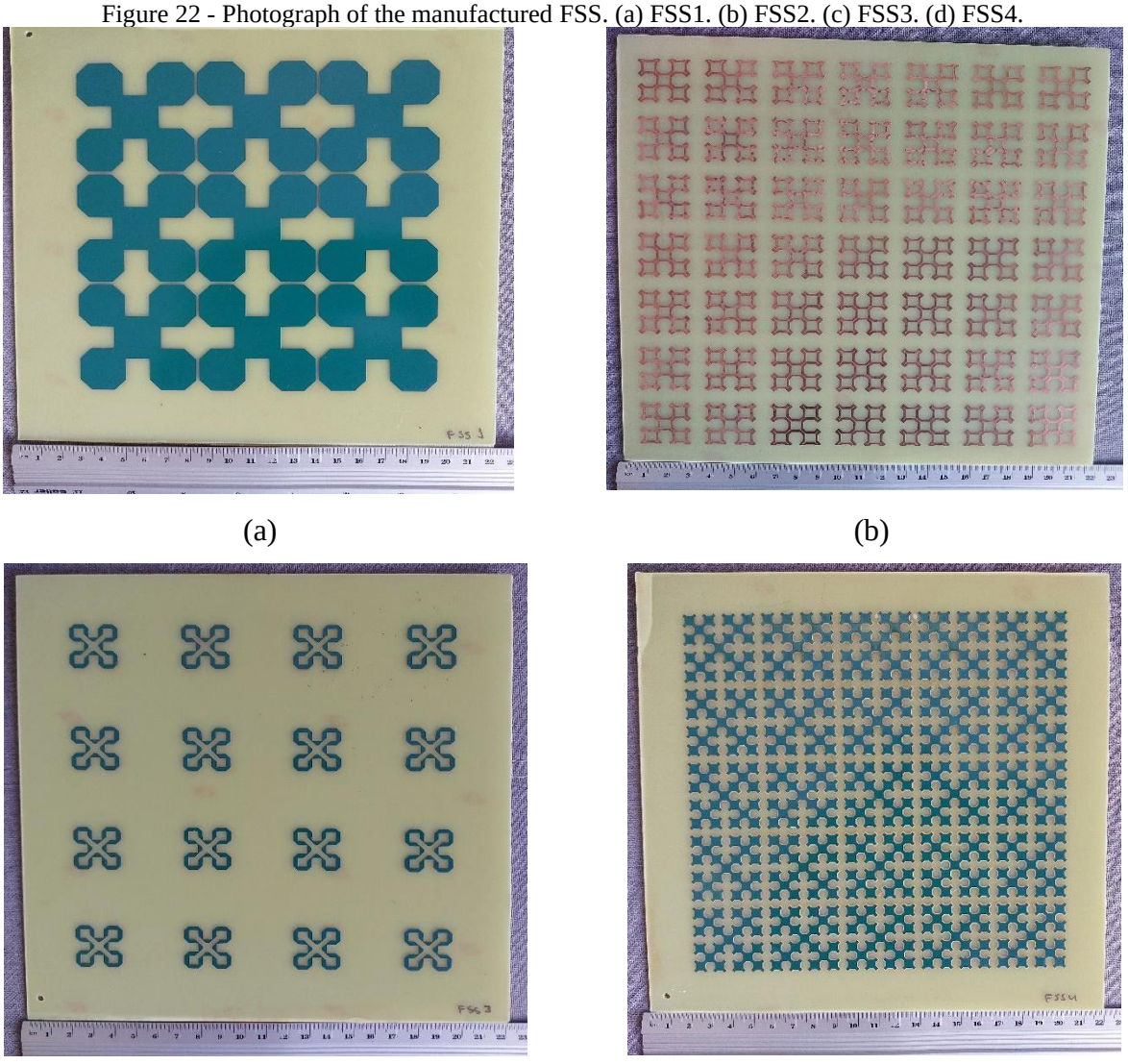

(a) (b)

(c) (d)

Source: The author.

# 6 ANALYSIS OF SIMULATED AND MEASURED RESULTS

In this chapter, the simulated results obtained using CST Microwave Studio software will be presented and compared with the measured results for the proposed system, consisting of the four fabricated FSS. Discussions regarding the small differences between the simulated and measured curves will be presented. Due to IFM systems requiring high-precision operation, and frequency selective surfaces being devices with frequency response sensitive to variations in the angle of wave incidence, it was decided to perform this study only with perpendicular wave incidence in order to maintain the high reliability of the developed discriminators.

## 6.1 SIMULATION RESULTS

The electromagnetic simulation software, CST Microwave Studio, was used for the electromagnetic compatibility design of the proposed FSS. The software applies the Finite Element Method for frequency-domain responses, approximating all simulated volumes in a tetrahedral structure. Figure 23 shows the structure of FSS 2 with the "Mesh View" function in the CST software activated and the representation of the simulation model for Port 1 ($z_{max}$))and Port 2 ($z_{min}$). In the case of a periodic structure, the cell to be simulated was multiplied, and all cells were approximated in a tetrahedral structure, as mentioned above. Initially, to obtain the required characteristics for the design, a threshold ($V_{th}$) was chosen for each FSS signal, which will later correspond to the bits for analog-to-digital conversion (A/D), determining whether the analyzed signal will be above or below this level.

Figure 23 - Image of the "Mesh View" function in the CST software active

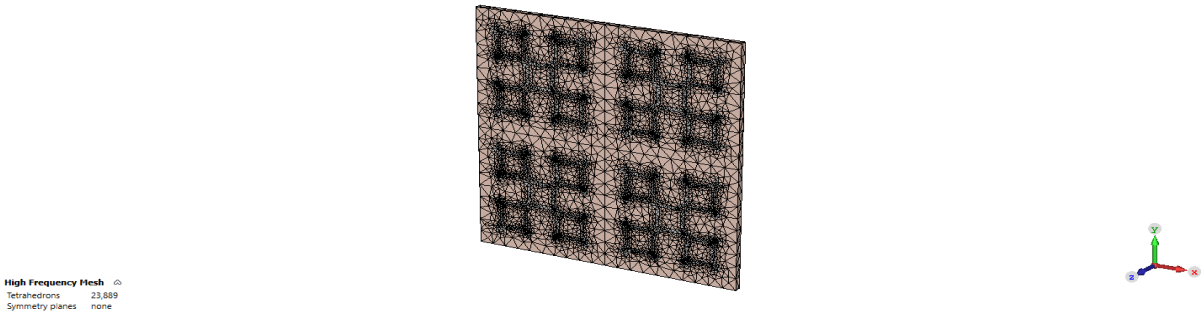


Source: The author.

The curves displaying the simulated results, specifically the transmission coefficient $S_{21}$ as a function of the operating frequency, are presented below, along with the indication of

the corresponding binary output to facilitate understanding. Figure 24 showcases the simulated result for FSS 1. The threshold was established at -7.09 dB. Consequently, Table 4 displays the frequency ranges along with their corresponding logic levels for FSS 1.

Figure 25 displays the simulated result for FSS 2. The threshold was set at -0.94 dB, and Table 5 represents the frequency ranges and corresponding logic levels. Similarly, Figure 26 presents the simulated result for FSS3. The threshold was established at -0.48 dB, and Table 6 showcases the frequency ranges and corresponding logic levels.

Lastly, Figure 27 exhibits the simulated result for FSS 4. The threshold was set at -7.71 dB, and Table 7 represents the frequency ranges and corresponding logic levels.

Therefore, the value of the signal power level is constantly compared to the predetermined power limit level (threshold) established in the design. If the value of the transmission coefficient ($S_{21}$) in decibels is greater than the threshold, the system will return the binary value "0". Similarly, if it is lower, it will return the binary value "1".

Table 4 - Frequency ranges and their corresponding logic levels for FSS 1

| Band (GHz) | | | Logic Level |
|---|---|---|---|
| 0.3926 | - | 0.97362 | 0 |
| 0.97362 | - | 2.8735 | 1 |
| 2.8735 | - | 4.5899 | 0 |
| 4.5899 | - | 5.3124 | 1 |
| 5.3124 | - | 5.5570 | 0 |

Source: The author.

Table 5 - Frequency ranges and their corresponding logic levels for FSS 2

| Band (GHz) | | | Logic Level |
|---|---|---|---|
| 0.3926 | - | 1.1447 | 0 |
| 1.1447 | - | 2.3031 | 1 |
| 2.3031 | - | 3.1298 | 0 |
| 3.1298 | - | 4.4849 | 1 |
| 4.4849 | - | 5.5570 | 0 |

Source: The author.

Table 6 - Frequency ranges and their corresponding logic levels for FSS 3

| Band (GHz) | | | Logic Level |
|---|---|---|---|
| 0.3926 | - | 1.9462 | 0 |
| 1.9462 | - | 3.2468 | 1 |
| 3.2468 | - | 4.3294 | 0 |
| 4.3294 | - | 4.9477 | 1 |
| 4.9477 | - | 5.5570 | 0 |

Source: The author.

Table 7 - Frequency ranges and their corresponding logic levels for FSS 4

| Banda (GHz) | | | Logic Level |
|---|---|---|---|
| 0.3926 | - | 1.3839 | 0 |
| 1.3839 | - | 2.1102 | 1 |
| 2.1102 | - | 3.8107 | 0 |
| 3.8107 | - | 5.5570 | 1 |

Source: The author.

Table 8 displays the identified sub-bands based on the simulation responses of the system composed of the four proposed FSS. Most of the sub-bands have a width of approximately 330 MHz. Due to small frequency shifts, some sub-bands may have variations, presenting values smaller or larger than 300 MHz. However, all 16 sub-bands have been identified, generally yielding good results. Thus, when a system provides a binary digital word such as "1011," it indicates that the input signal's frequency falls within the fourteenth sub-band of the system, within a frequency range between 4.6917 and 5.0224 MHz, consequently with a bandwidth of 330.7 MHz.

Figure 24 - Simulated result for FSS 1

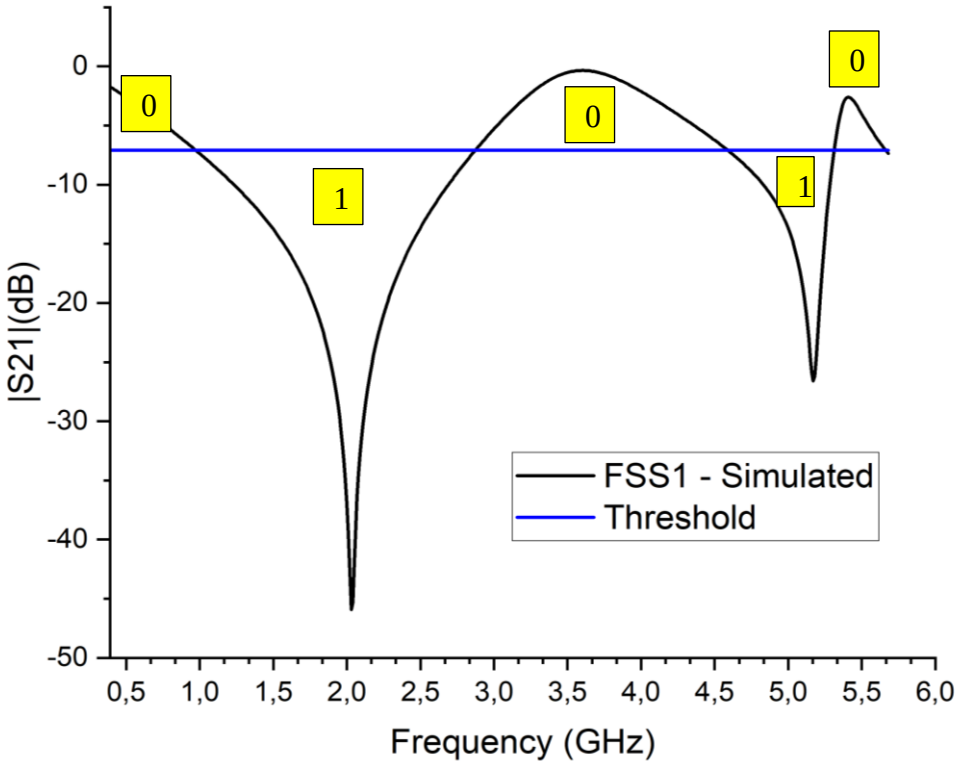


Source: The author.

Figure 25 - Simulated result for FSS 2

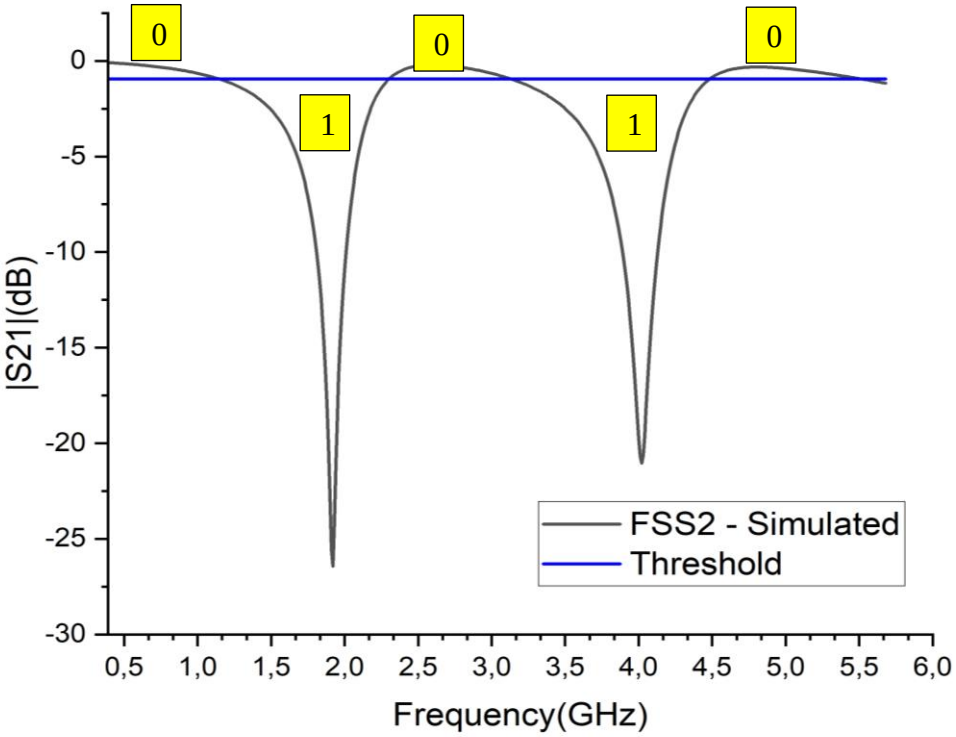


Source: The author.

Figure 26 - Simulated result for FSS 3

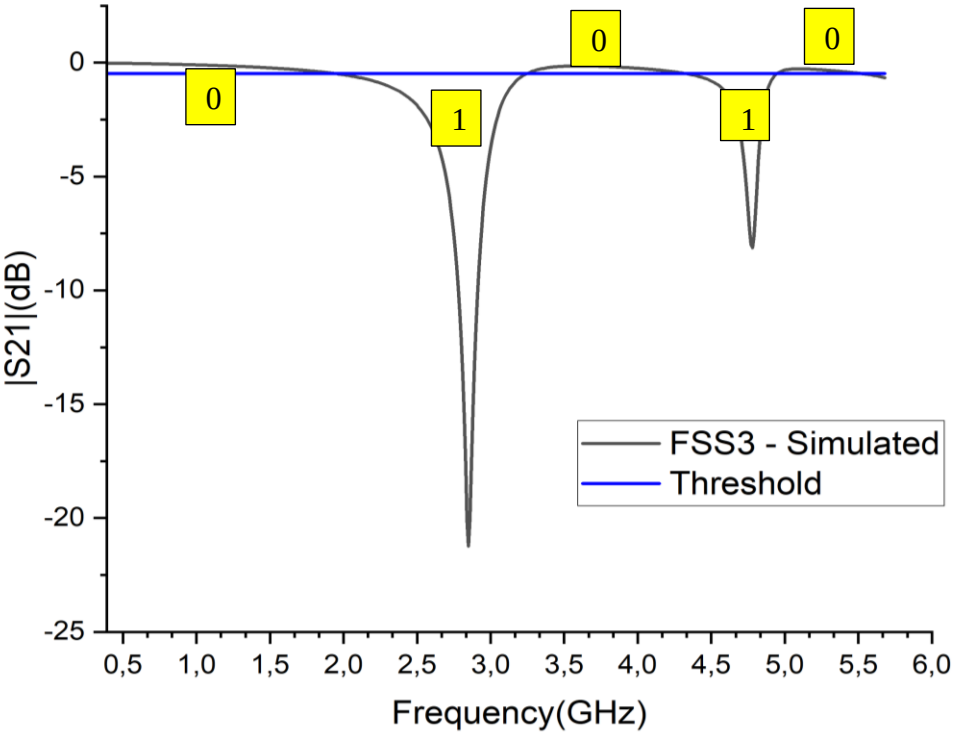


Source: The author.

Figure 27 - Simulated result for FSS 4

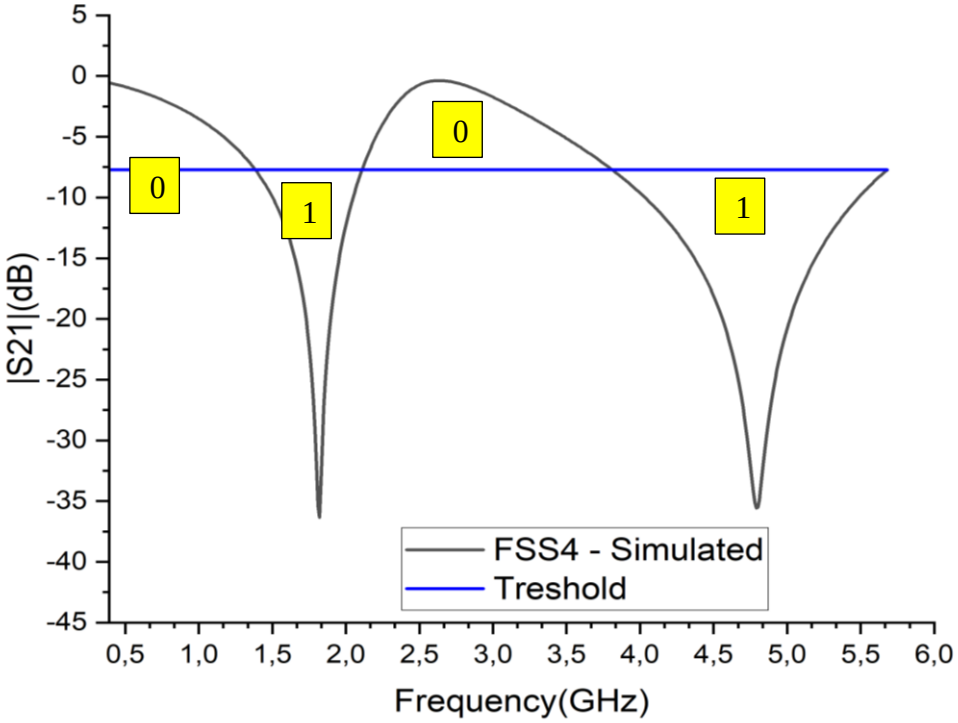


Source: The author.

Table 8 - Identified sub-bands and digital words of the four proposed FSS obtained from the simulated results

| **Sub-bands** | **Balanced Binary Representation** | **Fmax -Fmin (GHz)** | **Bandwidth (GHz)** |
|---|---|---|---|
| 1 | 0000 | 0.3926 to 0.9736 | 0.5810 |
| 2 | 1000 | 0.9736 to 1.1447 | 0.1711 |
| 3 | 1100 | 1.1447 to 1.3839 | 0.2392 |
| 4 | 1101 | 1.3839 to 1.9462 | 0.5623 |
| 5 | 1111 | 1.9462 to 2.1102 | 0.1640 |
| 6 | 1110 | 2.1102 to 2.3031 | 0.1929 |
| 7 | 1010 | 2.3031 to 2.8735 | 0.5704 |
| 8 | 0010 | 2.8735 to 3.1298 | 0.2563 |
| 9 | 0110 | 3.1298 to 3.2468 | 0.1170 |
| 10 | 0100 | 3.2468 to 3.8107 | 0.5639 |
| 11 | 0101 | 3.8107 to 4.3294 | 0.5187 |
| 12 | 0111 | 4.3294 to 4.4849 | 0.1555 |
| 13 | 0011 | 4.4849 to 4.5899 | 0.1050 |
| 14 | 1011 | 4.5899 to 4.9477 | 0.3578 |
| 15 | 1001 | 4.9477 to 5.3124 | 0.3647 |
| 16 | 0001 | 5.3124 to 5.5570 | 0.2446 |

Source: The author.

In Figure 28, we can clearly identify the relationship between the sub-bands, with their respective bandwidths.

Figure 28 - Bandwidths associated with the sub-bands for the simulated proposed IFM system

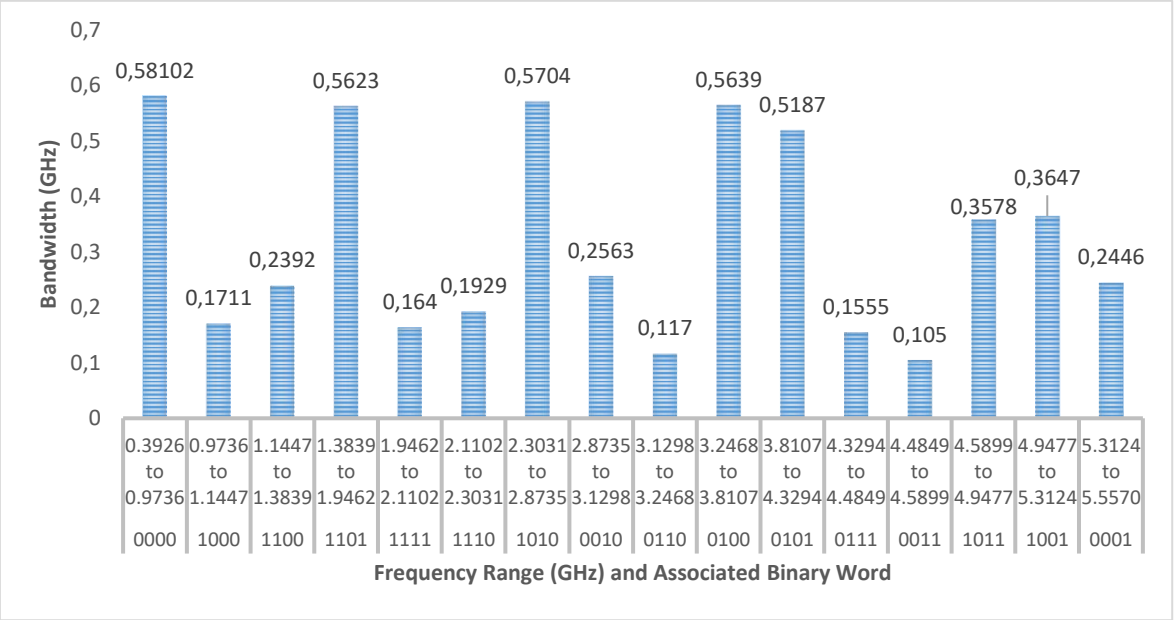


Source: The author.

## 6.2 EXPERIMENTAL SETUP FOR MEASUREMENTS

This section presents the experimental setup for the measurement of the proposed FSS considering normal incidence of a vertically and horizontally polarized plane wave, as depicted in Figure 29. The experimental results were obtained using a vector network analyzer, Agilent E5071C, and two double ridge guide horn antennas, model SAS-571, with operating frequency range of 700 MHz to 18 GHz, all connected by suitable coaxial cables and adapters for measuring the magnitude of the transmission coefficient, |S21|. The measurement setup comprises a panel with a 20 cm x 20 cm slot for attaching the FSS using transparent adhesive tapes, which do not interfere with the results, and pyramid absorbers surrounding the structure, as can be observed in Figure 30. All measurements were carried out at the Telecommunications and Applied Electromagnetics Group (GTEMA) at the Federal Institute of Paraíba (IFPB).

Figure 29 - Sketch of the system for measurements of the FSS

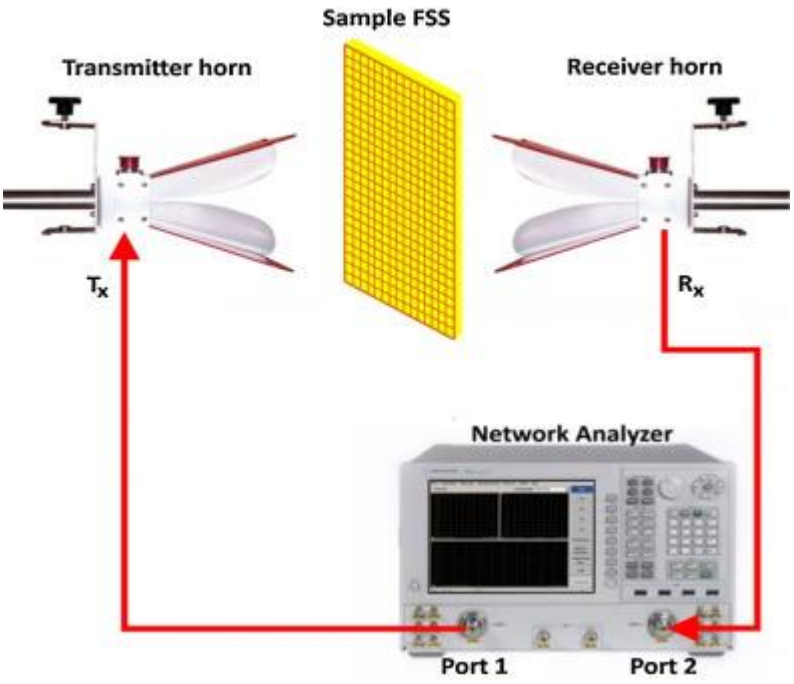


Source: [55]

In order to ensure greater accuracy of the experiment, the measurement of the system was obtained through two steps: first, for system calibration, the transmission without the FSS prototype is measured within the frequency range of interest, and then the FSS prototype is inserted between the two antennas, positioned at the center of the beam path, and the transmissions are measured and calibrated using the first result.

To standardize the measurements and ensure that the FSS were in the far-field region, a fixed spacing of 1.2 m was established between the two antennas. Two measurement configurations can be observed in Figure 30, representing the measurement setup for FSS 2. Since the measurement setup is identical for all FSS, the setups for the measurements of the other FSS will not be presented in this work.

Figure 30 - Experimental measurement of FSS 1 using a vector network analyzer

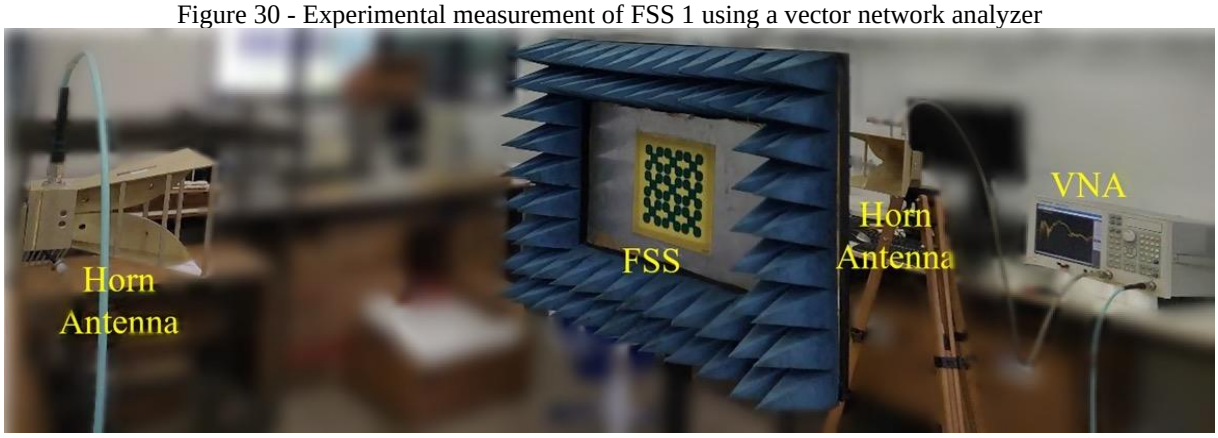


Source: The author.

## 6.3 EXPERIMENTAL RESULTS

Figures 31 to 34 show the experimental results of the four FSS compared to the simulated results. We observe that FSS 2 (Figure 32) and FSS 4 (Figure 34) exhibited excellent agreement between the simulated and measured results, with a small displacement, but without affecting the detection of the desired bits. Subsequently, we observe the comparisons for FSS 1 (Figure 31) and FSS 3 (Figure 33), which showed a slightly larger displacement. However, as we will see later, by adjusting the power threshold level and the bandwidths corresponding to each binary word, it is possible to adjust these parameters to obtain frequency responses that satisfactorily cover the entire frequency range in which the device operates.

Figure 31 - Comparison between the measured and simulated results of FSS 1.

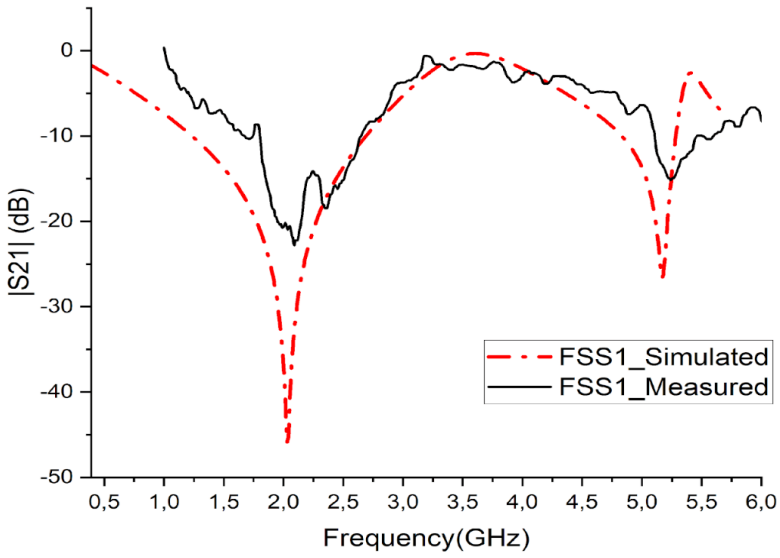


Source: The author.

Figure 32 - Comparison between the measured and simulated results of FSS 2

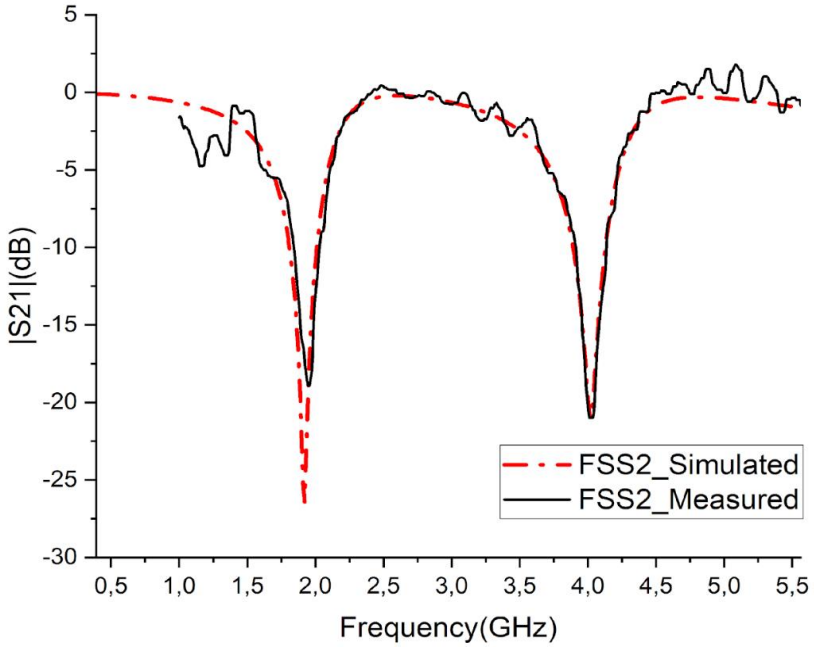


Source: The author.

Figure 33 - Comparison between the measured and simulated results of FSS 3

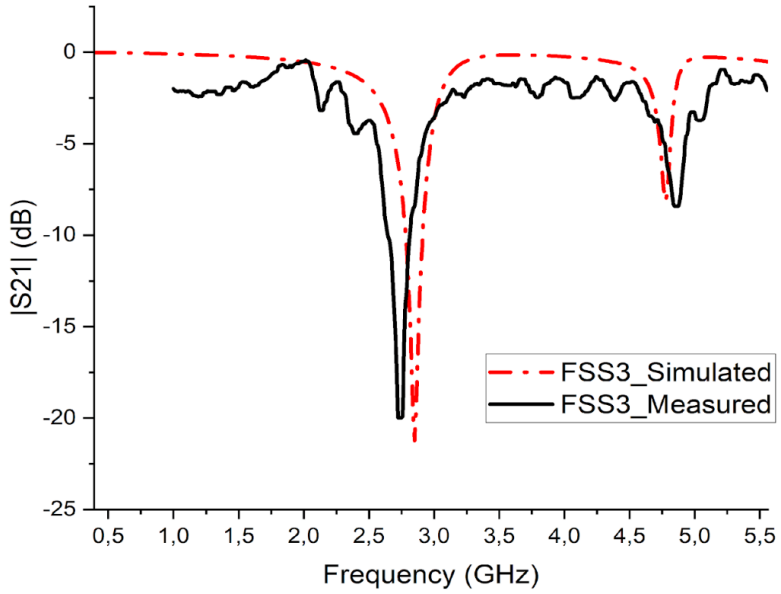


Source: The author.

Figure 34 - Comparison between the measured and simulated results of FSS 4

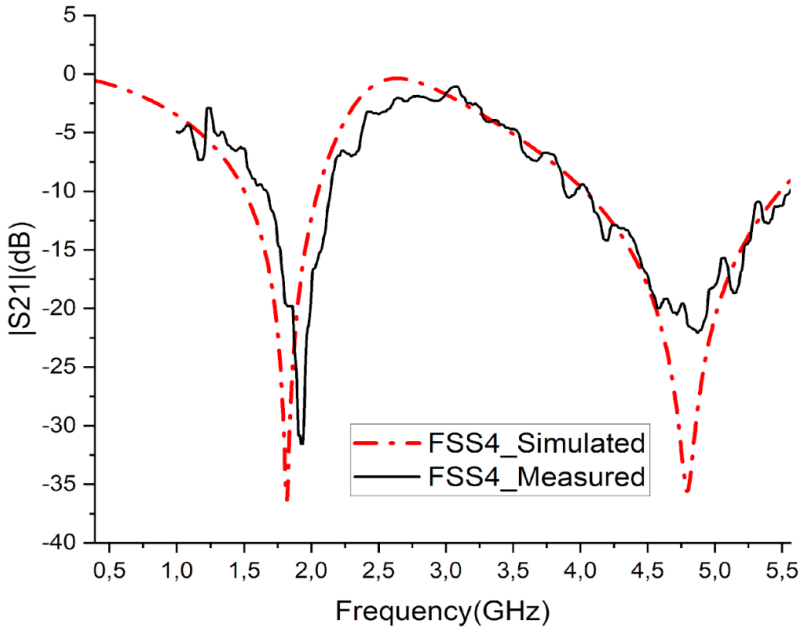


Source: The author.

Although small, the variations between the designed frequency response and the measured device responses alter the behavior of band identification in the system. Therefore, based on these results, it is necessary to readjust the parameters to optimize the system response. Therefore, a new table with the new transition frequencies for the formation of binary words was created based on the values obtained after the measurements. Table 8, as mentioned earlier, represents the values for the simulated configuration of the proposed device. On the other hand, Table–9 presents the new frequencies obtained after analyzing the curves from the system measurement, and Figure 35 shows the comparisons between the values of the simulated and measured curves.

From the measured results represented in Table 9, it can be observed that the discriminators start operating from 1.175 GHz, which is different from the simulated devices that start at 0.39 GHz. This is due to the measurement process of the FSS, as the frequency response of the SAS 571 horn antennas used begins at 700 MHz, and they have low gain at the beginning of the operating range, resulting in imprecise results. Therefore, to ensure the correct operation of the measured devices, the operating range according to Table 9 was used.

Despite the displacements in the operating bands of the FSS, i.e., the differences found between the simulated and measured values, the experimental results show that these devices can be used as discriminators in a simple 4-bit IFM system operating in the frequency range of 1.175 GHz to 5.56 GHz.

Analogously to tables 4, 5, 6, and 7, tables 8, 9, 10, and 11 demonstrate the frequency ranges and their corresponding logic levels for the measured results of FSS 1, FSS 2, FSS 3, and FSS 4, respectively.

Table 9 - Frequency ranges and their corresponding logic levels for FSS 1 - Measured.

| Band (GHz) | | | Logic Level |
|---|---|---|---|
| 1.175 | - | 2.925 | 1 |
| 2.925 | - | 4.549 | 0 |
| 4.549 | - | 5.557 | 1 |

Source: The author.

Table 10 - Frequency ranges and their corresponding logic levels for FSS 2 - Measured.

| Band (GHz) | | | Logic Level |
|---|---|---|---|
| 1.175 | - | 2.323 | 1 |
| 2.323 | - | 3.142 | 0 |
| 3.142 | - | 4.458 | 1 |
| 4.458 | - | 5.557 | 0 |

Source: The author.

Table 11 - Frequency ranges and their corresponding logic levels for FSS 3 - Measured.

| Band (GHz) | | | Logic Level |
|---|---|---|---|
| 1.175 | - | 2.113 | 0 |
| 2.113 | - | 3.247 | 1 |
| 3.247 | - | 4.374 | 0 |
| 4.374 | - | 5.095 | 1 |
| 5.095 | - | 5.557 | 0 |

Source: The author.

Table 12 - Frequency ranges and their corresponding logic levels for FSS 4 - Measured.

| Band (GHz) | | | Logic Level |
|---|---|---|---|
| 1.175 | - | 1.525 | 0 |
| 1.525 | - | 2.183 | 1 |
| 2.183 | - | 3.828 | 0 |
| 3.828 | - | 5.557 | 1 |

Source: The author.

Table 13 - Digital Words of the four proposed FSS obtained from the measured results.

| BALANCED BINARY REPRESENTATION | Fmin – Fmax (GHz) | BANDWIDTH (GHz) |
|---|---|---|
| 1100 | 1.175 to 1.525 | 0.350 |
| 1101 | 1.525 to 2.113 | 0.588 |
| 1111 | 2.113 to 2.183 | 0.070 |
| 1110 | 2.183 to 2.323 | 0.140 |
| 1010 | 2.323 to 2.925 | 0.602 |
| 0010 | 2.925 to 3.142 | 0.217 |
| 0110 | 3.142 to 3.247 | 0.105 |
| 0100 | 3.247 to 3.828 | 0.581 |
| 0101 | 3.828 to 4.374 | 0.546 |
| 0111 | 4.374 to 4.458 | 0.084 |
| 0011 | 4.458 to 4.549 | 0.091 |
| 1011 | 4.549 to 5.095 | 0.546 |
| 1001 | 5.095 to 5.557 | 0.462 |

Source: The author.

In Figure 35, we can clearly see the relationship between the sub-bands and their bandwidths, similar to what is observed in Figure 28, which represents the simulated system.

Figure 35 - Bandwidths associated with the sub-bands for the simulated proposed IFM – measured.

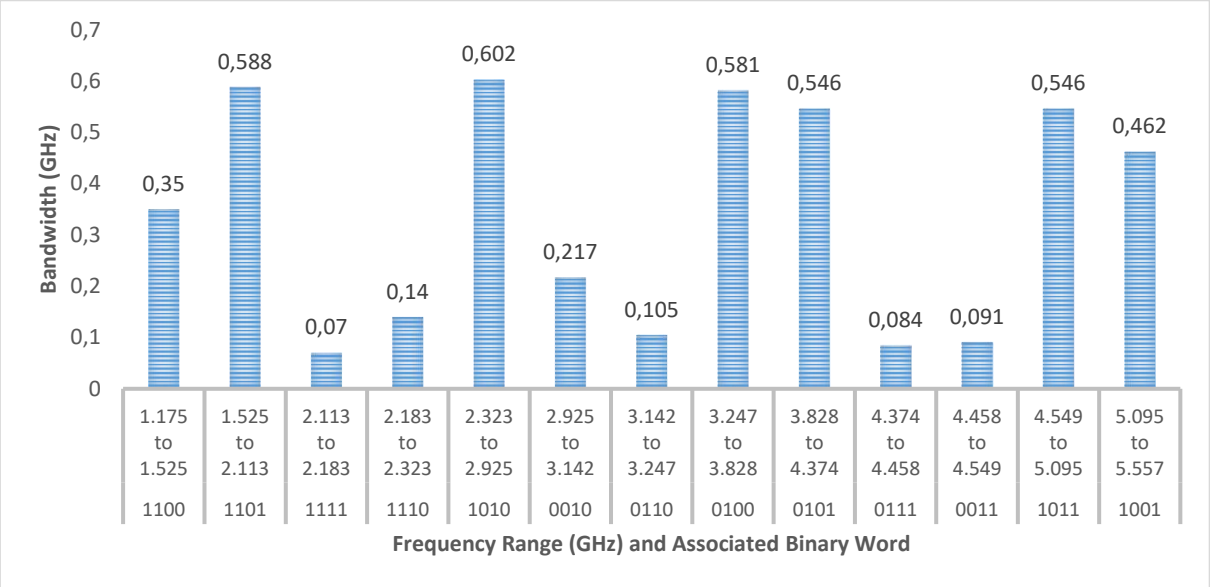


Source: The author.

The thresholds chosen for the four manufactured FSS were -4.520 dB, -0.824 dB, -2.552 dB, and -7.468 dB, respectively.

In the face of the presented threshold values, it is necessary to ensure that the signal passing through the frequency discriminators reaches the detector with power levels within the

device's operating range. In this context, tables 14, 15, 16, and 17 demonstrate the simulated power level values of each FSS at frequencies where the threshold line crosses the frequency response line to serve as a reference, and therefore, where bit transitions occur (1 to 0 or 0 to 1).

Table 14 - Transition Frequencies and Power levels - FSS 1

| Frequency (GHz) | Power level (dBm) |
|---|---|
| 3.0583 | **-26.112 (min)** |
| 4.549 | -14.096 |

Table 15 - Transition Frequencies and Power levels - FSS 2

| Frequency (GHz) | Power level (dBm) |
|---|---|
| 2.323 | **7.541 (máx)** |
| 3.142 | -0.344 |
| 4.458 | -16.420 |

Table 16 - Transition Frequencies and Power levels - FSS 3

| Frequency (GHz) | Power level (dBm) |
|---|---|
| 2.113 | -17.531 |
| 3.247 | -9.516 |
| 4.374 | -11.326 |
| 5.095 | -6.744 |

Table 17 - Transition Frequencies and Power levels - FSS 4

| Frequency (GHz) | Power level (dBm) |
|---|---|
| 1.525 | -21.782 |
| 2.183 | -9.606 |
| 3.828 | -5.152 |

According to the tables, the converter to be used in the system needs to have a minimum input level lower than -26.112 dBm at a frequency of 3.0583 GHz and a maximum input level higher than 7.5409 dBm at a frequency of 2.323 GHz in order to cover the entire range of bit transitions from the four frequency discriminators.

In the market, there are several detector models that meet these requirements, such as the ADL5511 model from the company Analog Devices, which has a minimum input level of

-30 dBm and a maximum input level of 17 dBm in the spectrum region near 2600 MHz, thus covering the necessary detection range for the proposed system. Further features, applications, and details of ADL5511 detector can be found in reference [56].

Another relevant analysis regarding the discriminators is their performance in relation to wave polarization. In this regard, it is worth noting that the symmetry of the Sierpinski Curve geometry allows for efficient operation with no significant differences for horizontally and vertically polarized incident waves. Figures 36, 37, 38, and 39 demonstrate a comparison between the measured results for the X polarization (XY - indicating that the antenna was oriented in the X axis direction) and the Y polarization (YY - indicating that the horn antenna was oriented in the Y axis direction).

Figure 36 - Comparison between the measured results for the X and Y polarization for FSS 1.

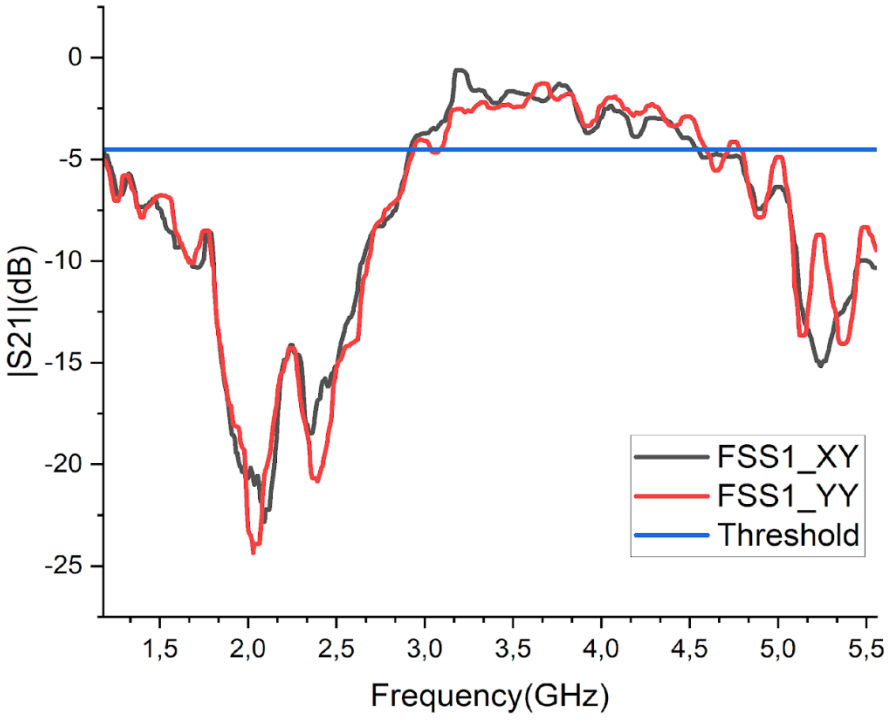


Source: The author

Figure 37 - Comparison between the measured results for the X and Y polarization for FSS 2.

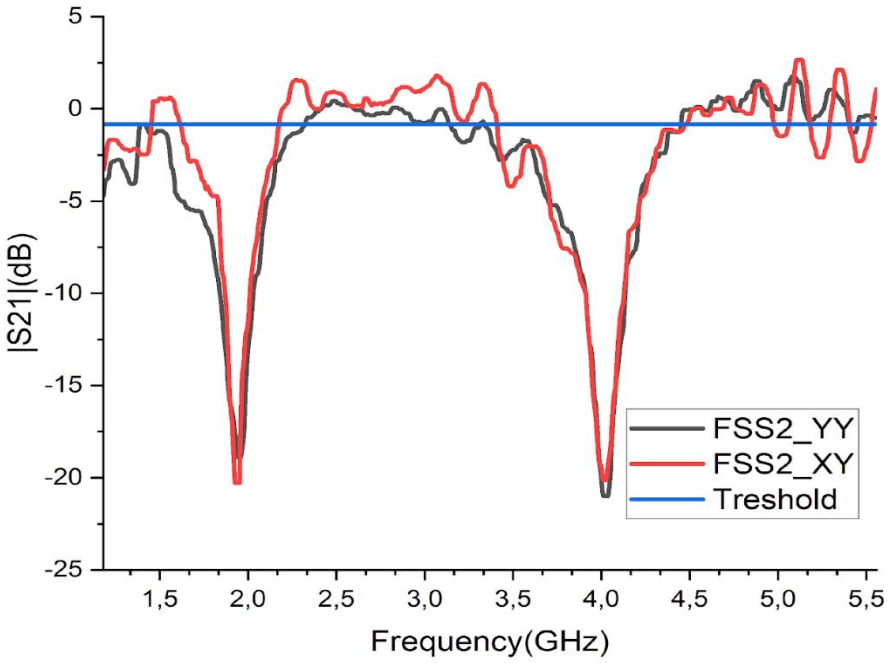


Source: The author

Figure 38 - Comparison between the measured results for the X and Y polarization for FSS 3.

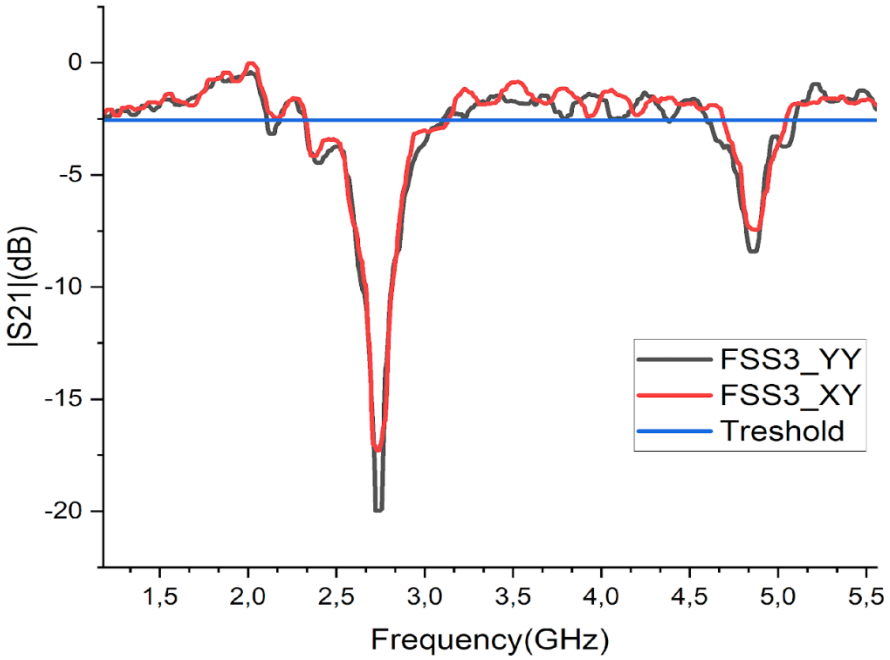


Source: The author.

Figure 39 - Comparison between the measured results for the X and Y polarization for FSS 4

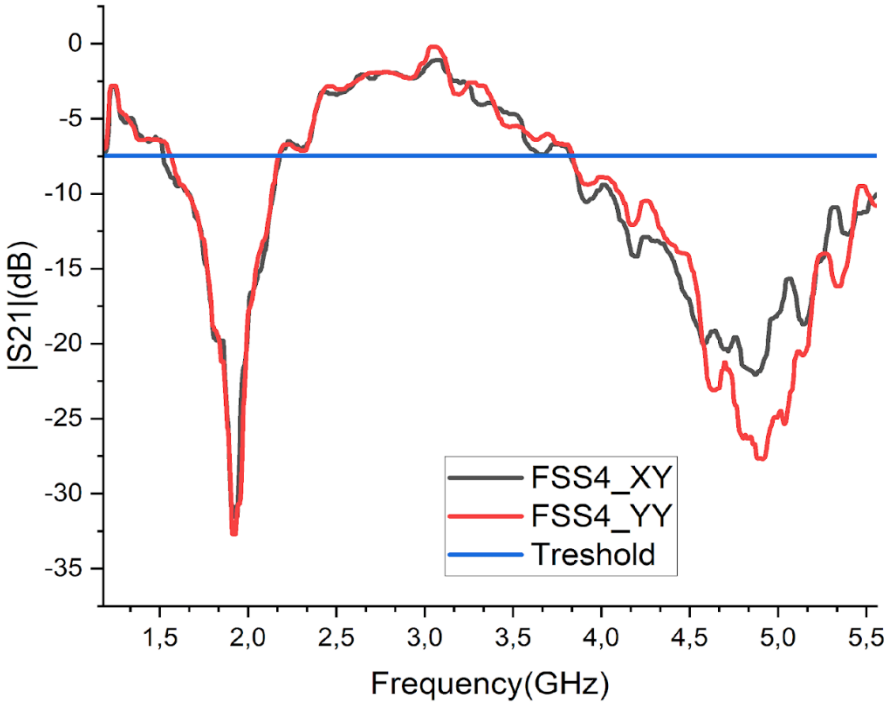


Source: The author.

# 7 POSSIBLE APPLICATION FOR THE DESIGNED DISCRIMINATORS

As explained, it is evident that the designed discriminators have several advantages compared to those previously presented in the literature. One notable advantage is the ability to operate with both vertical and horizontal linear polarizations. As previously mentioned, the symmetry of the geometry used in the design of the frequency selective surfaces allows for equal efficiency for horizontally and vertically polarized incident waves.

Based on this, it is possible to conjecture various applications for an IFM system that uses such discriminators, especially in aviation. Here are two possible main applications:

## 7.1 DUAL-POLARIZATION (POLARIMETRIC) RADARS

Dual-polarization radars, such as the METEOR 1500, transmit and receive radar pulses in horizontal (H) and vertical (V) polarizations [57]. By analyzing the differences between the returns in these polarizations, valuable information about the detected targets can be obtained. The Differential Reflectivity (ZDR), calculated from the H and V reflectivities, is useful for hail detection, for example. The dielectric constants of ice and water are also relevant, allowing for the distinction between different hydrometeors. These radars improve the detection and forecasting of hazardous weather events[58].

Figure 40 - Meteor 1500 CLP05 antenna

Source: [57]

Figure 41 - Correspondence between ZDR values and the size of a raindrop

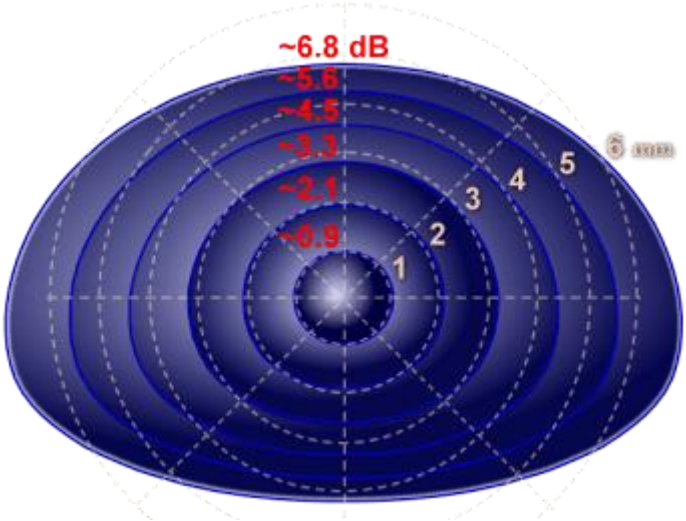


Source: [58]

In the frequency range from 1.175 GHz to 5.56 GHz, which corresponds to the frequency range of the frequency discriminators proposed in this work, there is an overlap with the frequency ranges of several dual-polarization weather radars. As examples, we have the Dual-Polarization S-Band Weather Radars (S-DPR), which operate in the frequency range of 2.7 GHz to 3.0 GHz, and the Dual-Polarization C-Band Weather Radars (C-DPR), which operate in the frequency range of 5.3 GHz to 5.6 GHz.

# 8 CONCLUSION

The present doctoral thesis implements the use of frequency selective surfaces with reject-band characteristics, based on the Sierpinski Curve fractal geometry, as frequency discriminators in digital Instantaneous Frequency Measurement (IFM) systems. The design parameter adopted to represent the output words was the Balanced Binary Code (BBC). Through a quantitative analysis, the benefits of using BBC (Balanced Binary Code) compared to Reflected Binary Code (RBC) were demonstrated, highlighting the potential for developing a 4-bit IFM (Instantaneous Frequency Measurement) system using only dual-band frequency discriminators.

Four dual-band FSS were developed and fabricated using a low-cost dielectric substrate. The theoretical and experimental results were carefully analyzed, and it was found that the frequency shifts obtained were minimal. By appropriately selecting the threshold levels for each state, the manufactured system was able to identify 13 distinct sub-bands within the range of 1.17 to 5.56 GHz, with an average bandwidth of 274 MHz. The choice of this number of sub-bands was based on the results obtained from the fabricated devices, taking into consideration the maintenance of the essential property of a 1-bit transition between consecutive words, even though a 4-bit system, in theory, could identify 16 distinct bands. However, the results clearly demonstrated that the proposed system is capable of performing its primary function, which is the instantaneous detection of the sub-band to which the input signal belongs.

It was possible to prove that replacing RBC with BBC results in a number of rejected bands equal to 2 for each discriminator, representing a design advantage for FSS, which becomes significantly more complex as a greater number of resonance frequencies is required.

Furthermore, the adoption of a fractal geometry in the design of FSS provided them with greater versatility, as no significant differences were observed between the responses to incident waves in vertical and horizontal polarizations. This opens up prospects for applications in areas such as weather radar systems, among others.

In summary, this doctoral thesis contributed to the advancement of research in frequency discriminators based on FSS for 4-bit IFM systems, demonstrating the advantages of using BBC compared to RBC, as used in [2]. The obtained results highlight the satisfactory performance of the designed fractal FSS, both from a theoretical and experimental standpoint, and indicate possibilities for application in various fields.

## 8.1 SUGESTION FOR FUTURE WORK

For future work, it is suggested to fabricate all the elements that make up the proposed IFM system, such as the UWB antennas operating in the system's operating range. The design and development of the digital system connected to the output of the A/D converter module, responsible for reading and interpreting the binary outputs, and the integration of all the mentioned elements that constitute the proposed simple IFM system. Additionally, measurements should be conducted in an anechoic chamber and tests carried out with the implemented system, followed by the design and development of the graphical user interface. Furthermore, due to the sensitivity of the FSS response to the angle of incidence of the incident wave, incorporating angle of incidence sensors into the system is suggested to further improve system accuracy. This enables real-time angle of incidence information and allows for dynamic adjustment of the system's parameters based on this information, using mathematical models such as adaptive algorithms, for example.

## 8.2 SCIENTIFIC PRODUCTION

As a result of the studies conducted during the completion of this doctorate, the research contributions generated, the results presented in this thesis, were produced directly or through collaborations developed in the microwave laboratory at UFPE. The following set of scientific publications, which includes an article published in a high-impact factor journal and several papers accepted at significant international conferences in the field, stems from these efforts.

1. **Cavalcanti Filho, P. H**., Araujo, J. A., de Oliveira, M. R. T., de Melo, M. T., Neto, A. G., & Coutinho, I. B. (2019, November). A new design of Sierpinski curve fractal FSS for S-band interference protection applications. In *2019 SBMO/IEEE MTT-S International Microwave and Optoelectronics Conference (IMOC)* (pp. 1-3). IEEE.

2. Araujo, J. A. I**., Cavalcanti Filho, P. H. B.**, de Oliveira, M. R. T., Silva, C. P. N., Llamas-Garro, I., de Melo, M. T., & Kleinau, B. A. (2019, November). A New Trapezium FSS Superstrate for Antenna Gain Enhancement. In *2019 SBMO/IEEE MTT-S International Microwave and Optoelectronics Conference (IMOC)* (pp. 1-3). IEEE.

3. **Cavalcanti Filho, P. H. B**., Araujo, J. A. I., Oliveira, M. R. T., de Melo, M. T., Coutinho, M. S., da Silva, L. M., & Llamas-Garro, I. (2020). Planar Sensor for Material Characterization Based on the Sierpinski Fractal Curve. *Journal of Sensors*, *2020*, 1-9.

4. SILVA, L. M. ; SILVA FILHO, H. V. H. ; **CAVALCANTI FILHO, P. H. B.** ; de Melo, M. T. . A new technique to cancel additional phase shifts of two-port resonant devices. In: Anais do Momag2020, 2020, VIRTUAL DEVIDO COVID19. ANAIS DO MOMAG 2020, **2020**. v. 1. p. 1-5.

5. Araujo, J. A. I., Oliveira, M. R. T., **Cavalcanti Filho, P. H. B.**, Silva, C. P. N., Coutinho, M. S., de Melo, M. T., ... & Barboza, A. G. (2021). Reconfigurable Filtenna using Varactor Diode for Wireless Applications. *Journal of Microwaves, Optoelectronics and Electromagnetic Applications*, *20*, 834-854.

## REFERENCES

[1] DE, Sampurna; BAZIL RAJ, A. A. A survey on photonics technologies for radar applications. **Journal of Optics**, v. 52, n. 1, p. 90-119, 2023.

[2] PINHEIRO, Giordano J. et al. Four-bit instantaneous frequency measurement systems based on frequency selective surfaces. **Microwave and Optical Technology Letters**, v. 61, n. 1, p. 68-72, 2019.

[3] KAPOOR, Ankush; MISHRA, Ranjan; KUMAR, Pradeep. Frequency selective surfaces as spatial filters: Fundamentals, analysis and applications. **Alexandria Engineering Journal**, v. 61, n. 6, p. 4263-4293, 2022.

[4] DE OLIVEIRA, Elias MF et al. A novel microstrip frequency discriminator for IFM based on balanced gray-code. In: **2017 SBMO/IEEE MTT-S International Microwave and Optoelectronics Conference (IMOC)**. IEEE, 2017. p. 1-4.

[5] DE OLIVEIRA, E. M. F. et al. A novel method for frequency discriminators construction based on balanced gray code. In: **2016 URSI Asia-Pacific Radio Science Conference (URSI AP-RASC)**. IEEE, 2016. p. 1482-1484

[6] OLIVEIRA, Elias Marques Ferreira de et al. Decodificação em identificadores instantâneos de frequência por Código Binário Balanceado. 2018. Tese de Doutorado. Universidade Federal de Pernambuco.

[7] KRZYSZTOFIK, Wojciech Jan; BRAMBILA, F. Fractals in antennas and metamaterials applications. **Fractal Analysis: Applications in Physics, Engineering and Technology**, p. 953-978, 2017.

[8] CAVALCANTI FILHO, Pedro HB et al. A new design of Sierpinski curve fractal FSS for S-band interference protection applications. In: **2019 SBMO/IEEE MTT-S International Microwave and Optoelectronics Conference (IMOC)**. IEEE, 2019. p. 1-3.

[9] MAGNUSSON, Philip C. et al. **Transmission lines and wave propagation**. CRC press, 2000.

[10] POZAR, David M. **Microwave engineering**. John wiley & sons, 2011.

[11] GOPAL, B. G.; RAJAMANI, V. Extraction of S parameter from EEHEMT nonlinear model of HJFET for X band. In: **2017 Conference on Emerging Devices and Smart Systems (ICEDSS)**. IEEE, 2017. p. 96-102.

[12] BAHL, Inder J. **Lumped elements for RF and microwave circuits**. Artech house, 2022.

[13] NYIKAYARAMBA, Gift; MURMANN, Boris. S-Parameter-Based Defect Localization for Ultrasonic Guided Wave SHM. Aerospace, v. 7, n. 3, p. 33, 2020.

[14] Link Communications Systems - VSAT Provider. **Link Communications Systems**. Available at: https://www.linksystems-uk.com/vsat-polarization. Accessed on: May 17th, 2023.

[15] DEGL'INNOCENTI, Egidio Landi; LANDOLFI, Marco. Description of Polarized Radiation. **Polarization in Spectral Lines**, p. 1-28, 2004.

[16] BAIER, Moritz Friedrich. **Polarization multiplexed photonic integrated circuits for 100 Gbit/s and beyond**. Technische Universitaet Berlin (Germany), 2018.

[17] STUTZMAN, Warren L. **Polarization in electromagnetic systems**. Artech house, 2018.

[18] GAO, Steven Shichang; LUO, Qi; ZHU, Fuguo. **Circularly polarized antennas**. John Wiley & Sons, 2014.

[19] TOCCI, Ronald J. **Digital systems: principles and applications**. Pearson Education India, 1991.

[20] RABIEE, Max. Parallel To Serial And Serial To Parallel Converters. In: **2002 Annual Conference**. 2002. p. 7.910. 1-7.910. 17.

[21] MUNK, Ben A. **Frequency selective surfaces: theory and design**. John Wiley & Sons, 2005.

[22] CAMPOS, Antônio Luiz Pereira de Siqueira. Superfícies seletivas em frequência: análise e projeto. 2008.

[23] AL-JOUMAYLY, Mudar A.; BEHDAD, Nader. Low-profile, highly-selective, dual-band frequency selective surfaces with closely spaced bands of operation. **IEEE Transactions on Antennas and Propagation**, v. 58, n. 12, p. 4042-4050, 2010.

[24] SAGAN, Hans. **Space-filling curves**. Springer Science & Business Media, 2012.

[25] BRUNI, Vittoria; DE CANDITIIS, Daniela; VITULANO, Domenico. Phase information and space filling curves in noisy motion estimation. **IEEE transactions on image processing**, v. 18, n. 7, p. 1660-1664, 2009.

[26] DE OLIVEIRA, M. R. T. et al. RFSS based on cross dipole or grid using PIN diode. **Microwave and Optical Technology Letters**, v. 59, n. 9, p. 2122-2126, 2017.

[27] CRNOJEVIC-BENGIN, Vesna; RADONIC, Vasa; JOKANOVIC, Branka. Fractal geometries of complementary split-ring resonators. **IEEE Transactions on Microwave Theory and Techniques**, v. 56, n. 10, p. 2312-2321, 2008.

[28] MITTRA, Raj; CHAN, Chi H.; CWIK, Tom. Techniques for analyzing frequency selective surfaces-a review. **Proceedings of the IEEE**, v. 76, n. 12, p. 1593-1615, 1988.

[29] CAVALCANTI FILHO, Pedro Henrique Bezerra et al. **FSS fractal baseada na geometria curva de Sierpinski para aplicações em sistema de radar**. 2018. Dissertação de Mestrado. Universidade Federal de Pernambuco.

[30] WU, T. K. Frequency Selective Surface and grid array (A Wiley Interscience publication). 1995.

[31] SILVA, H. V. H. et al. Multiband FSS with fractal characteristic based on Jerusalem cross geometry. **Journal of Microwaves, Optoelectronics and Electromagnetic Applications**, v. 16, p. 932-941, 2017.

[32] OLIVEIRA, Manuelle Regina Tavares de et al. Filtro reconfigurável baseado em RFSS tipo dipolo cruzado e grade. 2018. Tese de Doutorado. Universidade Federal de Pernambuco.

[33] LUCENA, Francisco Ariaildo CS et al. Gain enhancement of dual-band antenna using square loop FSS. In: **2017 IEEE International Symposium on Antennas and Propagation & USNC/URSI National Radio Science Meeting**. IEEE, 2017. p. 2169-2170.

[34] LANGLEY, Richard J.; PARKER, Edward A. Double-square frequency-selective surfaces and their equivalent circuit. **Electronics Letters**, v. 17, n. 19, p. 675-677, 1983.

[35] LEE, Chi Kwan; LANGLEY, R. J. Equivalent-circuit models for frequency-selective surfaces at oblique angles of incidence. In: **IEE Proceedings H (Microwaves, Antennas and Propagation)**. IET Digital Library, 1985. p. 395-399.

[36] PARKER, Edward A.; VARDAXOGLOU, J. C. Plane-wave illumination of concentric-ring frequency-selective surfaces. In: **IEE Proceedings H (Microwaves, Antennas and Propagation)**. IET Digital Library, 1985. p. 176-180.

[37] MITTRA, Raj; HALL, R.; TSAO, Chich-Hsing. Spectral-domain analysis of circular patch frequency selective surfaces. **IEEE transactions on antennas and propagation**, v. 32, n. 5, p. 533-536, 1984.

[38] BASSINGTHWAIGHTE, James B.; LIEBOVITCH, Larry S.; WEST, Bruce J. **Fractal physiology**. Springer, 2013.

[39] GNEITING, Tilmann; ŠEVČÍKOVÁ, Hana; PERCIVAL, Donald B. Estimators of fractal dimension: Assessing the roughness of time series and spatial data. **Statistical Science**, p. 247-277, 2012.

[40] LLAMAS-GARRO, Ignacio; KIM, Jung-Mu; DE MELO, Marcos Tavares. **Frequency measurement technology**. Artech House, 2017.

[41] ESPINOSA-ESPINOSA, M. et al. Reconfigurable frequency identification receivers. In: **2015 IEEE 15th Mediterranean Microwave Symposium (MMS)**. IEEE, 2015. p. 1-4.

[42] GOMES MOURA DE OLIVEIRA, Bruno. **Integração de Discriminadores de Frequência Para Sistemas IFM**. 2014. Tese de Doutorado. Universidade Federal de Pernambuco.

[43] SILVA, C. P. N. et al. Compact fractal interferometers for a 4-bit IFM system. **Microwave and Optical Technology Letters**, v. 59, n. 5, p. 1153-1157, 2017.

[44] ESPINOSA-ESPINOSA, M. et al. 4-bit, 1 to 4 GHz reconfigurable discriminator for frequency measurement. In: **2014 9th European Microwave Integrated Circuit Conference**. IEEE, 2014. p. 652-655.

[45] DE SOUZA, M. F. A.; E SILVA, F. R. L.; DE MELO, M. T. A novel LSB discriminator for a 5 bit IFM subsystem based on microstrip band-stop filter. In: **2008 38th European Microwave Conference**. IEEE, 2008. p. 36-39.

[46] DE OLIVEIRA, B. G. M. et al. Integrated instantaneous frequency measurement subsystem based on multi-band-stop filters. In: **2014 Asia-Pacific Microwave Conference**. IEEE, 2014. p. 910-912.

[47] DE OLIVEIRA, Elias MF et al. A novel microstrip frequency discriminator for IFM based on balanced gray-code. In: **2017 SBMO/IEEE MTT-S International Microwave and Optoelectronics Conference (IMOC)**. IEEE, 2017. p. 1-4.

[48] RAHIMPOUR, Hamid; MASOUMI, Nasser. Design and implementation of a high-sensitivity and compact-size IFM receiver. **IEEE Transactions on Instrumentation and Measurement**, v. 68, n. 7, p. 2602-2609, 2018.

[49] RAHIMPOUR, Hamid; MASOUMI, Nasser. High-resolution frequency discriminator for instantaneous frequency measurement subsystem. **IEEE Transactions on Instrumentation and Measurement**, v. 67, n. 10, p. 2373-2381, 2018.

[50] RAHIMPOUR, Hamid et al. A high frequency resolution successive-band shifted filters architecture for a 15-bit IFM receiver. **IEEE Transactions on Microwave Theory and Techniques**, v. 67, n. 5, p. 2028-2035, 2019.

[51] ESPINOSA-ESPINOSA, Moises et al. 2-Bit, 1–4 GHz reconfigurable frequency measurement device. **IEEE Microwave and wireless components letters**, v. 24, n. 8, p. 569-571, 2014.

[52] SILVA, Crislane Priscila do Nascimento et al. Interferômetro e sensor multibanda baseados na curva fractal de Hilbert. 2020. Tese de Doutorado. Universidade Federal de Pernambuco.

[53] CAVALCANTI FILHO, Pedro HB et al. A new design of Sierpinski curve fractal FSS for S-band interference protection applications. In: **2019 SBMO/IEEE MTT-S International Microwave and Optoelectronics Conference (IMOC)**. IEEE, 2019. p. 1-3.

[54] Rare Implementations: Sierpinski's Curve. **Piratefsh.github.io**. Available at: https://piratefsh.github.io/2020/08/08/sierpinski-curve.html. Accessed on: January 21th, 2023.

[55] MAJIDZADEH, Maryam; GHOBADI, Changiz; NOURINIA, Javad. Novel single layer reconfigurable frequency selective surface with UWB and multi-band modes of operation. **AEU-International Journal of Electronics and Communications**, v. 70, n. 2, p. 151-161, 2016.

[56] DC to 6 GHz ENVELOPE AND TruPwr™ RMS Detector. **ADL5511**. Available at:< https://www.analog.com/en/products/adl5511.html#product-overview>. Accessed on: June 27th, 2023.

[57] Noções Básicas de Radar. **Meteor 1500C**. Available at: www.radartutorial.eu, www.radartutorial.eu/19.kartei/10.weather/karte005.pt.html. Accessed on: May 27th, 2023.

[58] Dual Polarization Radar. **Radartutorial**. Available at: www.radartutorial.eu, www.radartutorial.eu/15.weather/wr51.en.html. Accessed on: April 17th, 2023.